skb.se

SKB P-22-08

ISSN 1651-4416

ID 1969287

November 2022

Parameter study of buffer upwards expansion into backfill

Buffer swelling against the backfill

Xavier Pintado
Mitta Oy

Keywords: buffer upwards, swelling pressure, inflow, dry density

Abstract

Buffer upwards swelling into the backfill is an important issue due to the reduction of the density and the swelling pressure of this barrier. This study presents the simulation of the buffer upwards as function of the backfill stiffness, water supply, dry density of the buffer blocks and friction in buffer – rock contact. The simulations were carried out in isothermal conditions and only the buffer components (blocks and pellets) were considered. The geometry was axisymmetric.

The results show large dependence on the backfill stiffness and blocks dry density and relatively small dependence on water supply and friction in buffer – rock contact.

Sammanfattning

Buffertens uppsvällning mot återfyllning är en viktig fråga på grund av dess sänkande effekt på buffertens torrdensitet och svälltryck. Denna studie presenterar en simulering av buffertuppsvällning som en funktion av återfyllningens styvhet, vattentillförsel, buffertblockens torrdensitet och väggfriktion vid gränsytan mellan buffert och berg. Simuleringar utfördes under isotermiska förhållanden och endast buffertkomponenterna (block och pellets) beaktades. Geometrin var axiellt symmetrisk.

Resultaten visar att återfyllningens styvhet och blockens torrdensitet hade ett stort beroende på buffertens uppsvällning. Vattentillförsel och friktion vid buffert/bergkontakten hade en relativt liten effekt.

Content

1 Introduction

SKB is currently reviewing its requirement on buffer upwards expansion into backfill to see if the requirements can be less strict by crediting friction against the rock walls in the deposition hole. In the current requirement, the backfill should have a compressibility that compares to a displacement of 15 cm with a pressure of 3.8 MPa. The requirement is calculated assuming no friction between the buffer and the deposition hole and is, therefore, very pessimistic. This approach causes that the requirement on the compressibility of the backfill to become very strict. In reality, it is likely that the friction between the buffer and the deposition hole will reduce the buffer swelling significantly. The idea is to see if it is possible to use some friction in the deposition hole to reduce the requirement on compressibility of the backfill.

To evaluate how large is the friction that can be accredited in the buffer, it is necessary to know how large the effect of the different parameters on the total friction is. For example, scale experiments (Sandén et al. 2020) have suggested that the buffer swelling is dependent on where the inflow in the deposition hole is located. To examine the effect of friction, it has been decided to model a simplified deposition hole and to do a parametric study carrying out a set of simulations to better understand how friction evolves when the buffer is swelling.

First, it was necessary to choose the constitutive models that should be used at the simulations. Mitta has worked in collaboration with CIMNE in the simulation of the hydration and swelling pressure development in KBS-3V buffer and backfill (Toprak 2018, Toprak et al. 2016, 2018). The constitutive model proposed for the buffer blocks is the Barcelona Basic Model (BBM; Alonso et al. 1990). This constitutive model has been used in the simulation of "in situ" tests related with buffer hydration and swelling (Chen and Ledesma 2009, Gens et al. 2009, Kristensson and Börgesson 2015, Rodríguez-Dono et al. 2020). The pellets were simulated with the Barcelona Expansive Model (BExM; Gens and Alonso 1992). This model was developed for dealing with expansive double structure clays and has already been used in the simulation of the KBS-3V buffer and backfill (Toprak et al. 2018). Finally, the contact between bentonite and the confining wall (metal or rock) was simulated with continuum elements using the Drucker-Prager constitutive model, with a friction angle of 7.2°, following the Mohr-Coulomb model taken from Dueck et al. (2019) as it is said in the Modelling assignment specification, and a null cohesion. The Drucker-Prager constitutive model (cone yield surface) is close to Mohr – Coulomb (non-regular pyramid with a hexagon base) in the expected stress state (compressive triaxial). Drucker-Prager constitutive model has also been used for the simulation of contacts with Abaqus computer code (Åkesson et al. 2010).

The models are implemented in CODE_BRIGHT computer code (DECA-UPC 2021), so this code was used for carrying out the simulations.

The simulations were hydro-mechanical (HM). This means that only the water mass balance and the stress equilibrium or momentum balance equations were solved. The variables were the liquid pressure (P_l) and the radial and axial displacements (u_r and u_z) because the geometry was axisymmetric, following the Modelling assignment specification.

This report contains two major parts: the parametrization of the model which includes a study of the wall friction modelling with three different methods and the results of the sensitivity analysis on buffer upwards due to buffer swelling as it was assigned in the project.

The material described in the Modelling assignment specification is MX-80. This material is a commercial name of Wyoming bentonite provided by American Colloid Company. Mitta has work with other Wyoming bentonites provided by other companies which can be described as MX-80-type, with the same properties (or similar, with the same variations expected in different batches of the original MX-80).

2 Cases description

The modelling work presented in this report consists of a Base case and ten different variations of the Base case divided in two parts, the Part 1 corresponding to the sensitivity analysis to boundary conditions (Table 4-2, six variations) and the Part 2 corresponding to the sensitivity analysis to buffer – rock friction (Table 4-3, four variations). The geometry was axisymmetric (Figure 2-1) and only radial and axial processes can be considered. The canister was not considered, so there were only blocks and pellets in the deposition hole. The flow of water was from the side boundary (Base case and four variations) or from the bottom (two variations) The water flow was simulated fixing null suction (s) in the water supply boundaries. The initial conditions were defined by the initial dry density and the initial water content (or initial degree of saturation in one of the variations).

The gas pressure (P_g) was constant with a value of 0.1 MPa, so the liquid pressure (P_l) fixed in the water supply boundaries was 0.1 MPa as well, so $s = P_g - P_l = 0$. In hydro-mechanical analysis, it can be null but if the temperature is considered, then the gas pressure should be fixed at 0.1 MPa. It was chosen to leave the files ready for considering the temperature and avoiding the mistake of carrying out the simulations with null gas pressure in non-isothermal conditions.

2.1 Initial conditions

The initial total stress was -0.11 MPa in axial, radial and circumferential senses (σ_r=σ_θ=σ_z=-0.11). The net stress is defined as σ_i-P_g where σ_i can be σ_r, σ_θ and σ_z and the initial value was -0.01 MPa. The constitutive models chosen have a logarithmic elastic part which depends strongly on the initial value, so it was considered necessary to agree this value like it was a part of the initial values of the assignment, like the initial density or the initial water content. CODE_BRIGHT computer code follows the continuous mechanics sign convention (tensile positive and compression negative), for this reason, the initial stresses are negative (compression).

The initial porosity, directly related with the initial dry density (see equation 3-5), depends on the case considered and it is described in Table 4-4, where the results are presented. The initial suction is related with the degree of saturation through the water retention curve (see sections 3.1.1 and 3.2.1). The initial degree of saturation can be calculated from the initial water content and the initial dry density (see equation 4-2). The initial suction is also described in Table 4-4.

2.2 Boundary conditions

The side boundary was fixed (no displacements neither in radial sense nor in axial sense) and the bottom boundary was fixed with rollers, allowing the sliding of the buffer on the rock (radial displacements) but not axial displacements. Allowing or not the sliding at the bottom does not change the results.

The backfill was represented as springs in the Base case and nine variations and just as a weight (constant axial pressure) in one variation. This weight was applied at the beginning of the calculations. The boundary condition with springs can be defined as:

$$\sigma_y = -0.11 - \gamma u_y \qquad (2\text{-}1)$$

where σ_y is the axial stress (MPa) in the contact buffer – backfill, u_y the axial displacements (m) and γ is the spring constant which has units of MPa/m or MN/m^3. The value of the constants used in this analysis are presented in Table 4-2. The stress of -0.11 MPa (compression of the buffer) is added to be in equilibrium with the initial stress state. The radial displacements were allowed like at the bottom of the deposition hole (rollers).

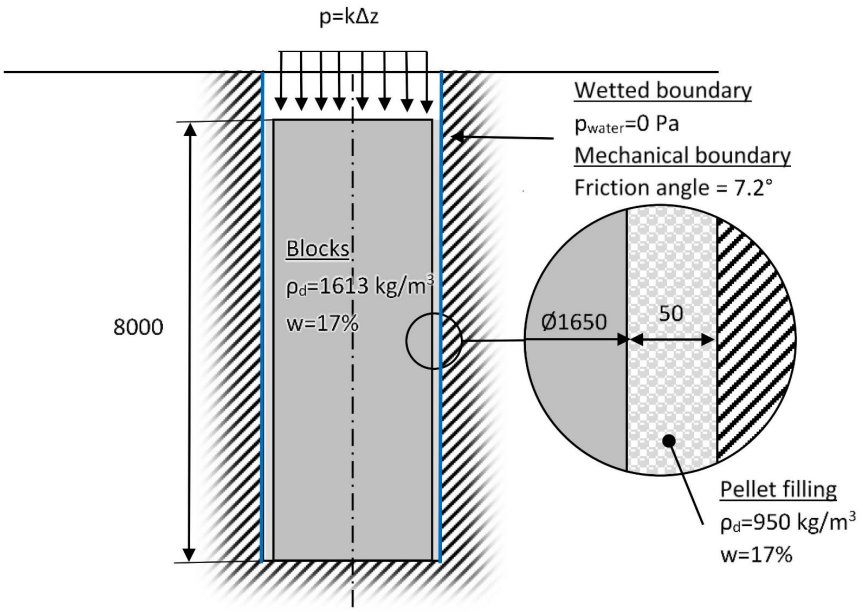

Figure 2-1. Illustration of the base case.

3 Constitutive models

Three different constitutive models were needed. The constitutive model for blocks, the constitutive model for pellets and the constitutive model for the joint. The rock was just the boundary.

The simulations were hydro-mechanical, so it was necessary to describe the hydraulic and mechanical parameters. The constitutive models for blocks and pellets were the Barcelona Basic Model (BBM, Alonso et al. 1990) and the Barcelona Expansive model (BExM, Gens and Alonso 1992) respectively. The Barcelona Basic model has been described extensively in different SKB reports (Åkesson et al. 2010, Kristensson and Börgesson 2015) and in articles related with SKB research projects (Åkesson et al. 2009, Chen and Ledesma 2010) and it will not be described in this report. The Barcelona Expansive model is also described extensively in Toprak (2018) and in Toprak et al. (2018) and it will not be described in this report either. The joint model will be described in Section 3.3.2.

The hydraulic constitutive laws are the Darcy's law for the liquid advective flow and the van Genuchten (1980) model for the water retention curve. The relative permeability follows the Brooks and Corey (1964) law. These laws and their implementation for the simulation of the water flow in the Engineered Barrier System (EBS) are described in the references given above for the description of the BBM and BExM.

There are some limitations in BBM due to the elastic parameters do not depend on the void ratio. This dependency could be considered indirectly although the best option is just to define a set of parameters for each void ratio keeping in mind that these parameters will not change during the hydration process. This statement is correct under constant volume conditions (swelling pressure test) but could be far from the real conditions when the strains are important (swelling under small axial load test).

3.1 Blocks

3.1.1 Hydraulic parameters

The hydraulic parameters are the water retention curve and the hydraulic conductivity.

The water retention curve can be measured without volumetric changes in wetting path (Dueck 2004, Villar 2005, 2007, Tang 2005, Seiphoori 2014, Pintado et al. 2013, Kiviranta et al. 2018; see Figure 3-1). When the sample dries, it shrinks and it is not possible to keep the volume constant. The constitutive models implemented in CODE_BRIGHT require the water retention curve measured in this condition. The water retention curve measured in free swelling conditions was provided by SKB in wetting, drying and mixed wetting-dry paths (Figure 3-1). The water retention curve measured without constant volumetric changes and in free swelling conditions coincide till the osmotic swelling (or double layer swelling) starts to be relevant, which happens when the suction is less than certain suction depending on the bentonite, 40 MPa in MX-80 (Navarro et al. 2015).

Although the measurement of the water retention curve presents large scatter, the measurements provided by SKB matches quite well with the measurements carried out by other authors (Figure 3-1). It should be taken into account that the measurements provided by SKB were done in powder samples and the other measurements were done in compacted samples at different dry densities.

The water retention curve chosen for the simulations was the van Genuchten (1980) water retention curve:

$$S_e = \frac{S_r - S_{rl}}{S_{ls} - S_{rl}} = \left(1 + \left(\frac{P_g - P_l}{P}\right)^{\frac{1}{1-\lambda}}\right)^{-\lambda} \quad (3\text{-}1)$$

Where P_g - P_l is the suction (the difference between gas pressure P_g and liquid pressure P_l), S_e is the effective degree of saturation, S_r the degree of saturation, S_{rl} the minimum degree of saturation and S_{ls} the maximum degree of saturation. In this report, it is considered S_{rl}=0 and S_{ls}=1, so S_e=S_r.

P is the air entry value and λ the shape factor, which depend on the porosity following the equations:

$$P(\phi) = P_0 \times exp\left(a_{ret} \times (\phi_0 - \phi)\right) \tag{3-2}$$

$$\lambda(\phi) = \lambda_0 \times exp\left(b_{ret} \times (\phi_0 - \phi)\right) \tag{3-3}$$

Where P_0 and λ_0 are the parameters when the porosity is ϕ_0 and a and b are parameters.

The parameter values are presented in Table 3-1.

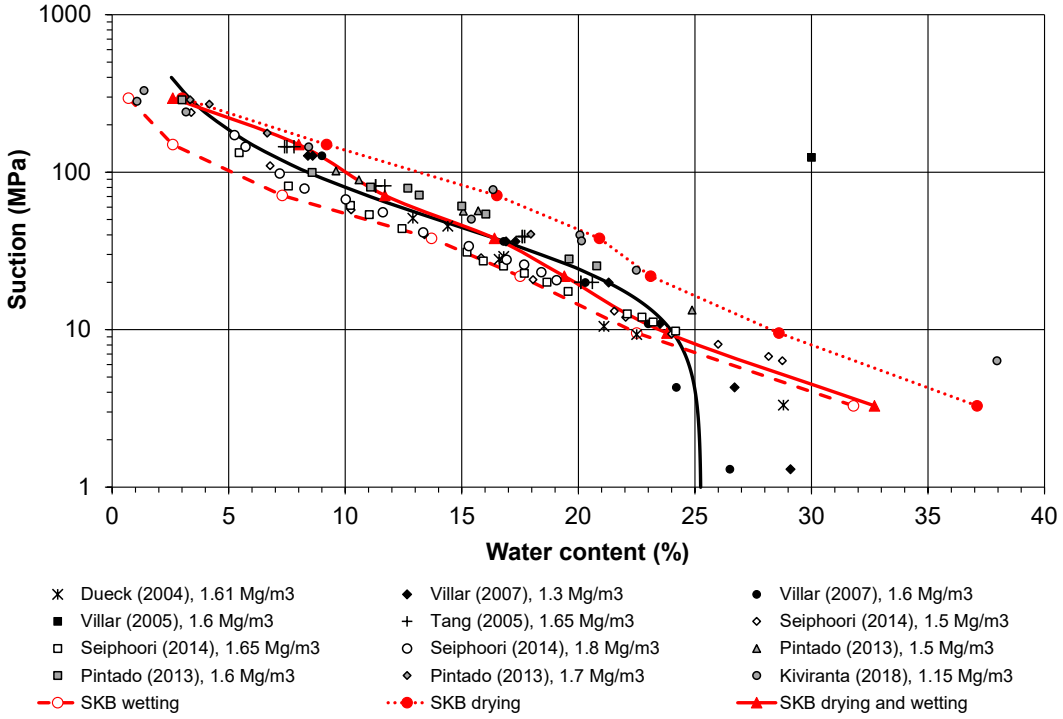

Figure 3-1. Water retention curve measurements and water retention curve chosen for the simulations (line in black).

The hydraulic conductivity is based on the data collected from different authors and also based on the data provided by SKB (Figure 3-2). The hydraulic conductivity (m/s) is around 10^7 times the intrinsic permeability (m^2) at temperatures around 20°C, which is function of the porosity ϕ following the equation

$$k(\phi) = k_0 \times exp\left(b_{hyd} \times (\phi - \phi_0)\right) \tag{3-4}$$

Where k_0 is the intrinsic permeability at porosity ϕ_0 and b_{hyd} is a parameter. Note that the porosity is directly related with the dry density following the equation

$$\phi = 1 - \frac{\rho_d}{\rho_{solids}} \tag{3-5}$$

The parameter values are presented in Table 3-1.

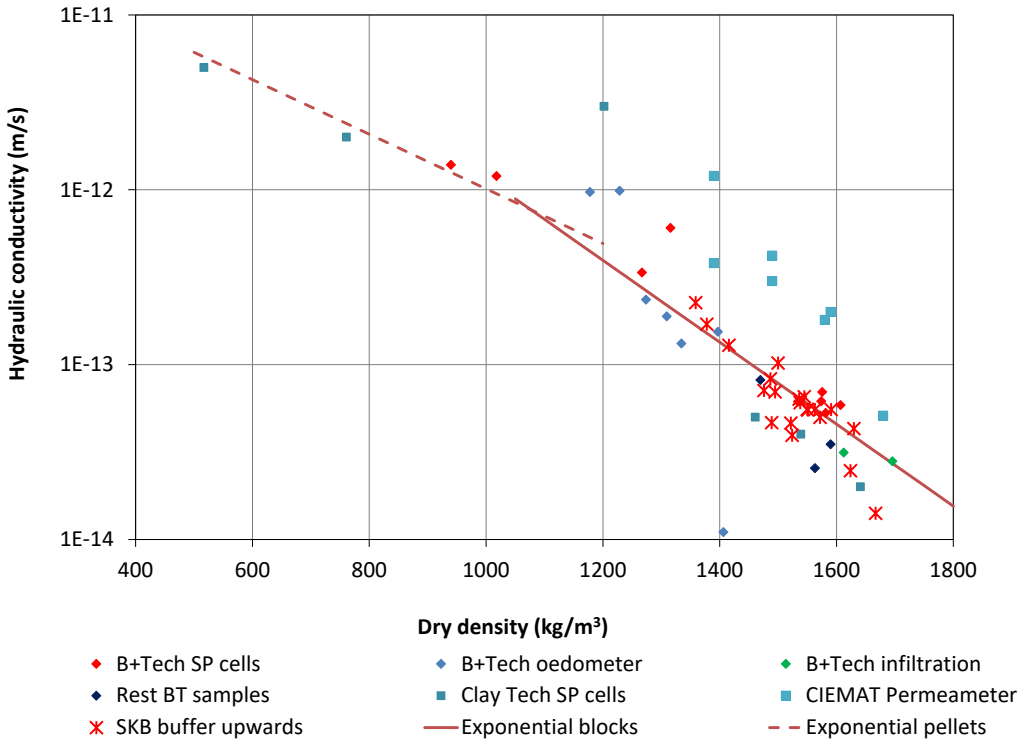

Figure 3-2. Hydraulic conductivity vs dry density. CIEMAT permeameter from Villar (2005), B+Tech SP cells (Schatz and Martikainen 2011 and Martikainen and Schatz 2011), Clay Tech SP cells (Karnland et al. 2006), B+Tech infiltration and B+Tech oedometers (Pintado and Rautioaho 2013), Rest BT samples (Pintado et al. 2018).

The relative hydraulic conductivity k_{rl} can be defined as (Brooks and Corey 1964)

$$k_{rl} = S_e^n \tag{3-6}$$

Where the exponent n was 3 (see Table 3-1). S_e was defined in the equation (3-1).

Table 3-1 Hydraulic parameters of blocks.

Van Genuchten[1] *(black line in Figure 3-1)*					**Darcy** *(exponential blocks line in Figure 3-2)*			***k**rl*
P_0 *(MPa)*	λ_0 *(-)*	a_{ret} *(-)*	b_{ret} *(-)*	ϕ_0 *(-)*	$k_0^{(1)}$ *(m^2)*	$b_{hyd}^{(1)}$ *(-)*	$\phi_0^{(1)}$ *(-)*	$n^{(2)}$ *(-)*
27	0.45	11	4	0.4245	5.6×10^{-21}	15	0.438	3

(1) Pintado et al. 2018, Toprak et al. 2018

(2) Chen and Ledesma 2010, Åkesson et al. 2009, 2010

3.1.2 Mechanical parameters

The blocks mechanical parameters were based on the parameters presented by Toprak et al. (2016) with two changes. The first one is related with κ_s, the parameter related with the elastic volumetric changes due to suction changes. The value calculated by Toprak et al. (2016) provides smaller values of swelling pressure. This value was calculated basically from oedometers, which have a different load path than the swelling pressure tests, where the volume remains constant.

The swelling pressure when 0.5<e<1.5 according to Börgesson et al. (1995) in tests where the sample was soaking keeping constant volume is

$$p = p_0 \cdot \left(\frac{e}{e_0}\right)^{(1/\beta)} \tag{3-7}$$

Where p_0 is the swelling pressure at e_0 and β is a parameter. The values in MX-80 bentonite are 1000 kPa. 1.1 and -0.19 respectively (Börgesson et al. 1995). Note that the initial suction is not considered in this equation due to the initial water content expected in blocks does not have influence on the swelling pressure. Some experimental points are compared with the relation proposed by Börgesson et al. (1995) (Figure 3-3). In order to be consistent with other SKB reports, the parameters of the equation (3-7) were not adjusted.

The mechanical parameters of blocks are presented in Table 3-2 and Table 3-3.

Table 3-2 Mechanical parameters of blocks (Toprak et al. 2016).

Parameter	Symbol	Value
Poisson ratio (-)	ν	0.3
Minimum bulk modulus (MPa)	K_{min}	10
Reference mean stress (MPa)	p_{ref}	0.01
Parameter for elastic volumetric compressibility against mean net stress change (-)	κ_{i0}	0.09
Parameter for elastic volumetric compressibility against suction change (-)	κ_s	Table 3-3[1]
Parameter for elastic thermal strain (°C^{-1})	α_0	9×10^{-4}
Slope of void ratio – mean net stress curve at zero suction	$\lambda(0)$	0.25
Parameter for the slope void ratio	r	0.8
Coefficient setting the change in cohesion with suction (MPa-1)	β	0.02
Reference pressure (MPa)	p^c	0.1
Pre-consolidation mean stress for saturated soil (MPa)	p_0^*	2
Tensile stress at zero suction (MPa)	p_{s0}	0.115[2]
Critical state line	M	0.36[2]

[1] Calibrated for this work

[2] Calibrated from Börgesson et al. (1995), Dueck et al. (2010) and Dueck and Nilsson (2010)

The κ_s values were calculated from simulations of the swelling pressure test (hydration of the bentonite without change of volume), where the initial conditions were the same the initial conditions of the cases simulated (dry density and water content).

Table 3-3 κ_s values.

Swelling pressure (MPa)	9.071	3.233	14.174
Initial suction (MPa)[1]	35.8	40.7	35.2
Void ratio (-)	0.723	0.880	0.665
Blocks dry density (kg/m^3)	1613	1479	1670
κ_s (-)	0.100	0.056	0.118

[1] The suctions are equivalent to 17 % water content at the different blocks dry densities

The second change was related with the shearing parameters, which were M=0.36 and p_{s0}=0.115 MPa, closer to results obtained in triaxial tests by Börgesson et al. (1995), Dueck et al. (2010) and Dueck and Nilsson (2010). Buffer upwards is mainly related with volumetric changes but the shearing can also play a certain role, especially when the buffer – rock friction is considered.

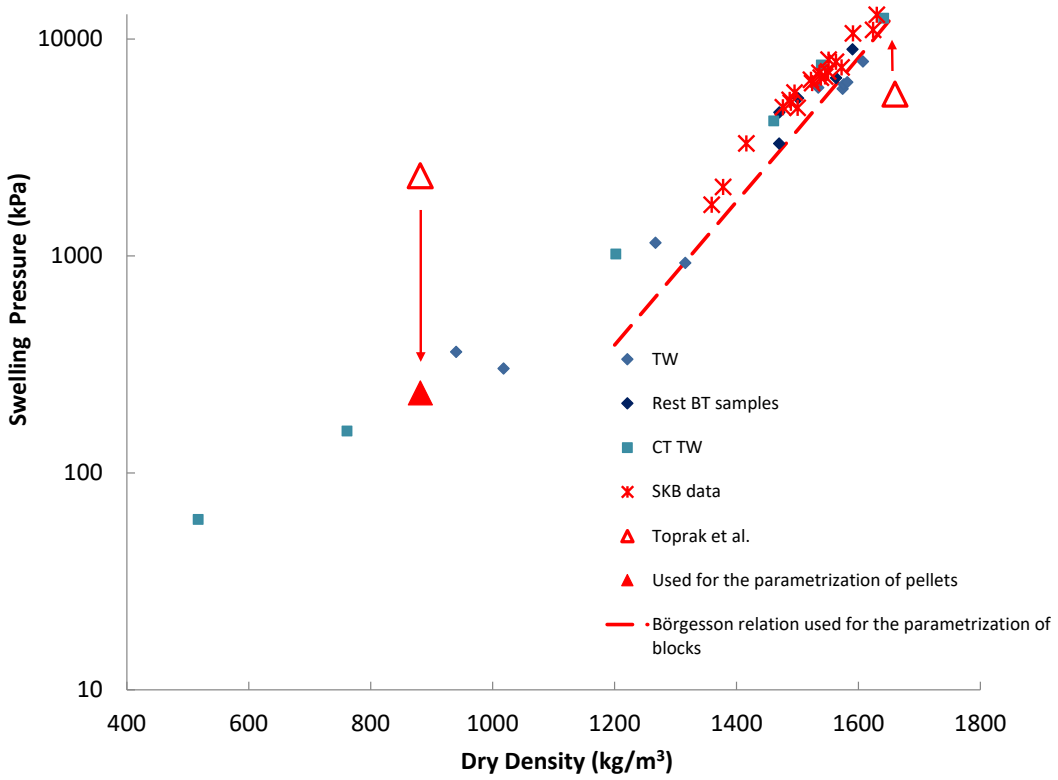

Figure 3-3. Swelling pressure vs dry density in samples saturated with tap water (TW: Schatz and Martikainen (2011) and Martikainen and Schatz (2011), Rest BT samples: Pintado et al. (2018), CT TW: Karnland et al. (2006), SKB data: Svensson et al. (2017)). Arrows indicate the change from Toprak et al. (2016, 2018) for blocks and pellets to the parametrization used in this work. Note that the swelling pressure of blocks was increased and in pellets was decreased.

The elastic part of the BBM model implemented in CODE_BRIGHT (DECA-UPC 2021) is able to carry out calculations with κ_i and κ_s functions of the net mean stress p' and suction s. These functions depend on a set of parameters (α_i, α_{il}, α_{sp}, α_{ss}) which have been used in past (Toprak et al. 2013) but these parameters should be used with caution due to small variations of these parameters might have large differences in the modelling results. This report has not used these parameters and were null in all calculations.

3.2 Pellets

3.2.1 Hydraulic parameters

The pellets water retention curve follows the van Genuchten equation (3-1) but the parameters are different because the relations (3-2) and (3-3) do not work when the differences in porosity are too large. The data and the retention curve can be seen in Figure 3-4. The parameters calculated are $P=P_0$=1.8 MPa and $\lambda=\lambda_0$=0.3.

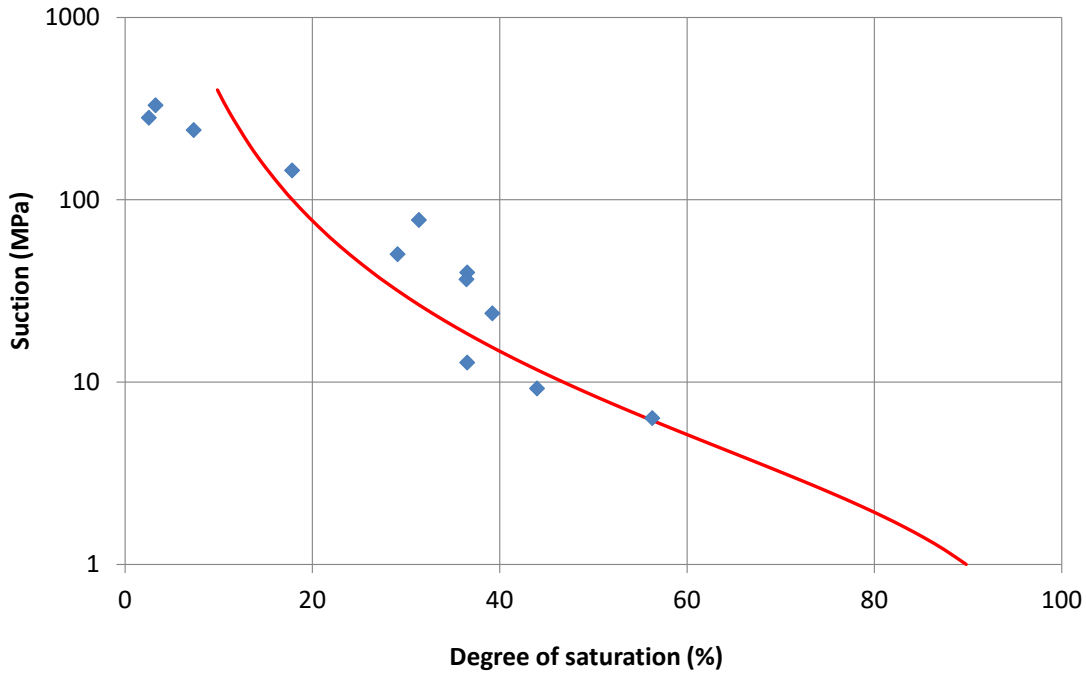

Figure 3-4. Swelling. Pellets water retention curve (modified data from Kiviranta et al. 2018).

The hydraulic conductivity follows the exponential law presented in the equation (3-4). The relation adjusted for the blocks might be used in pellets as well due to there is not large divergence when the dry density is 950 kg/m^3 (see Figure 3-2) but it was decided to use a closer relation, where the parameters were k_0=10^{-19} m^2, ϕ_0=0.8 and b_{hyd}=10 (Toprak et al. 2018 with a correction in ϕ_0).

The relative permeability is identical to blocks'. The hydraulic parameters of pellets are presented in Table 3-4.

Table 3-4 Hydraulic parameters of pellets.

Van Genuchten		Darcy			k_{rl}
P_0 (MPa)	λ_0 (-)	k_0	b_{hyd} (-)	ϕ_0 (-)	n (-)
1.8	0.3	10^{-19}	10	0.8	3

3.2.2 Mechanical parameters

The pellets constitutive model was the BExM with the parameters presented in Toprak et al. (2018) with the correction in volumetric swelling parameters of the κ_s=0.0008 instead 0.01 and κ_{micro}=0.004 instead 0.09 in order to reduce the swelling (see Figure 3-3). The shear parameters were also modified, with M=0.36 and p_{t0}=0.115 MPa. The mechanical parameters of the pellets are presented in Table 3-5.

Table 3-5 Mechanical parameters of pellets (Toprak et al. 2018).

Parameter	Symbol	Value
Parameter for elastic volumetric compressibility against mean net stress change of the macro (-)	κ^{macro}	0.045
Parameter for elastic volumetric compressibility against mean net stress + suction change of the micro (-)	κ^{micro}	0.004[(1)]
Parameter for elastic volumetric compressibility against suction change of the macro (-)	κ_s^{macro}	0.0008[(1)]
Minimum bulk modulus of the macro (MPa)	K_{min}^{macro}	10
Minimum bulk modulus of the micro (MPa)	K_{min}^{macro}	0.001
Poisson ratio (-)	ν	0.3
Parameter for elastic thermal strain (°C^{-1})	α_0	1×10^{-5}
Suction decrease interaction function parameter	f_{SD0}	-0.1
Suction decrease interaction function parameter	f_{SD1}	1.1
Suction decrease interaction function parameter	n_{SD}	2
Suction increase interaction function parameter	f_{SI0}	-0.1
Suction increase interaction function parameter	f_{SI1}	0.5
Suction increase interaction function parameter	n_{SI}	1
Slope of void ratio – mean net stress curve at zero suction	$\lambda(0)$	0.19
Parameter for the slope void ratio	r	0.8
Coefficient setting the change in cohesion with suction (MPa-1)	β	0.0001
Reference pressure (MPa)	p^c	0.1
Pre-consolidation mean stress for saturated soil (MPa)	p_0^*	2
Tensile stress at zero suction (MPa)	p_{t0}	0.115[(2)]
Critical state line	M	0.36[(2)]

(1) Calibrated for this work

(2) Calibrated from Börgesson et al. (1995), Dueck et al. (2010) and Dueck and Nilsson (2010)

3.3 Joint

Three different options were considered for the implementation of the friction: Joint material between the buffer and the rock (finally used in Base case and its variations), zero-thickness elements between the buffer and the rock and springs simulating the rock.

Joint material

The joint material is a continuous material with small thickness in order to minimize the influence of its dimension. In this case and for avoiding possible problems due to if the Lagrangian updated mesh option is used, the size of the joint material was 25 mm but choosing a suitable Poisson ratio (ν) for reducing the volumetric strains. It is not possible to fix the Young modulus and the shear modulus (G) for avoiding radial displacements but allowing shear strains. This is due to the elastic parameters are the Young modulus (E) and the Poisson ratio. The shear modulus can be defined with a value of the Poisson ratio close to 0.5, so

$$G = \frac{E}{2(1+\nu)} \tag{3-8}$$

The value of Poisson ratio close to 0.5 only becomes the material incompressible, increasing the bulk modulus (K) following the equation

$$K = \frac{E}{3(1-2\nu)} \tag{3-9}$$

This means that although the volumetric strain can be almost null, the radial strains could not be negligible if they are compensated with circumferential and axials strains. Only if the model allows to fix the Young and the shear modulus might be possible to avoid radial strains but, in this case, with large Young modulus and small value of the shear modulus, the value of the Poisson ratio could be out of the range [-1, 0.5].

$$\nu = \frac{E}{2G} - 1 \tag{3-10}$$

The joint model used in this work was viscoplastic. The elastic part was homogeneous and it is defined by the Young modulus and the Poisson ratio. The relations between these two parameters and the bulk modulus and the shear modulus are presented in the equations 3-8, 3-9 and 3-10.

The viscoplastic strain rate is defined by

$$\dot{\boldsymbol{\varepsilon}}^p = \Gamma\langle\Phi(F)\rangle\frac{\partial G}{\partial \boldsymbol{\sigma}} \tag{3-11}$$

Where Γ is a parameter related with the fluidity of the material, F is the yield surface, G is the plastic potential and $\Phi(F)$ is a stress function defined as

$$\Phi(F) = F^m \tag{3-12}$$

The parameter Γ depends on the temperature but due to this modelling was isothermal, it was constant.

This model is equivalent to Drucker – Prager model, where

$$F = q - \delta p' - c\beta \tag{3-13}$$

$$G = q - \delta\alpha p' - c\beta \tag{3-14}$$

c is the cohesion, α is the parameter δ=M (CSL in BBM model), δ and β are related with the friction angle defined in Mohr-Coulomb constitutive model by

$$\delta = M = \frac{6\,sin\phi'}{3 - sin\,\phi'} \tag{3-15}$$

$$\beta = \frac{6\,cos\phi'}{3 - sin\,\phi'} \tag{3-16}$$

Due to the cohesion was considered null, the β parameter did not play any role in this work. The values of the parameters are presented in Table 3-6. More information about how to model the discontinuities with the continuous material in CODE_BRIGHT can be found in DECA-UPC (2020).

Zero-thickness elements

The zero-thickness elements are also implemented in CODE_BRIGHT. In this case, the normal and the shear stresses are function of the normal and shear displacements and not function of the normal and shear strains.

$$\begin{bmatrix}\sigma' \\ \tau\end{bmatrix} = \begin{bmatrix}K_n & 0 \\ 0 & K_s\end{bmatrix}\begin{bmatrix}u_n \\ u_s\end{bmatrix} \tag{3-17}$$

Where $K_n = \frac{m}{a - a_{min}}$, m is the stiffness in normal sense (MPa), a is the opening aperture and a_{min} the minimum aperture (m). K_s is the shear stiffness (MPa/m).

The yield function is defined as:

$$F = \tau^2 - (c' - \sigma_n' tan\phi')^2 \tag{3-18}$$

Where τ is the shear stress, c' is the effective cohesion, σ_n' is the net normal stress and ϕ' is the friction angle. More information about the implementation of the zero-thickness elements and how to use can be found in Zandarin (2010) and Zandarin et al. (2011).

Springs

The boundary condition can also be implemented using springs. In this case, it is not necessary to implement any joint material but it is not possible to consider plasticity.

The 2-D boundary conditions in CODE_BRIGHT can now be defined as:

$$u_1 = u_x cos(\alpha_1) + u_y cos(\beta_1) \tag{3-19}$$

$$u_2 = u_x cos(\alpha_2) + u_y cos(\beta_2) \tag{3-20}$$

$$f_y = f_y^0 + \gamma cos(\beta_1)(u_1^0 - u_1) + \gamma cos(\beta_2)(u_2^0 - u_2) \tag{3-21}$$

Where u_1 and u_2 are the displacements in two directions, α_1 and α_2 are the angles of the directions respect to x-axis, β_1 and β_2 are the angles of the two directions respect the y-axis, f_y is the nodal force in MN and γ(MN/m) is a parameter. The boundary condition can also be fixed considering stresses, so f_y becomes σ_y and the constant γ is defined in MN/m^3. If the displacements at certain direction must be null, γ should be large (10^{10} by default in CODE_BRIGHT). CODE_BRIGHT was modified in order to be able to consider the boundary conditions fixing not only the velocities (DECA-UPC 2021) but also the displacements as well.

In lateral boundary (buffer – rock contact) $cos(\alpha_2)$ and $cos(\beta_1)$ are null,

$$u_1 = u_x cos(\alpha_1) \tag{3-22}$$

$$u_2 = u_y cos(\beta_2) \tag{3-23}$$

Then, if f_y^0 , u_1^0 and u_2^0 are also null,

$$f_y = -\gamma cos(\beta_2) u_y cos(\beta_2) = -\gamma \big(cos(\beta_2)\big)^2 u_y \tag{3-24}$$

It is possible to define a constant spring if the direction of u_2 and u_y are the same (y-axis). The constant of the spring is $\gamma\big(cos(\beta_2)\big)^2$ and will be defined in Section 3.3.2. The value of γ is already fixed with the default value due to $u_1=u_x=0$, and $cos(\alpha_1)=1$.

It is important to point out that this boundary condition cannot consider the plasticity of the joint, so the shear stiffness increases and the plasticity depends on the material in contact with the boundary, the pellets in this case.

Another important point is the sign of γ in CODE_BRIGHT. As flag, the value should be negative if the boundary conditions are fixed as function of the displacements. The document considers the sign positive, the negative value does not have physical sense.

3.3.1 Hydraulic parameters

The hydraulic parameters of the joint should not disturb the saturation process expected from the boundary conditions. When water flows from the side boundary, the hydraulic conductivity of the joint should be large for allowing the flow from the rock to the buffer. An alternative that was used is to impose the rock liquid pressure in both sides of the joint. When water flows from the bottom, the joint should have low hydraulic conductivity in order to avoid axial water flow through the boundary. In this case, the joint intrinsic permeability was 10^{-23} m^2, two orders of magnitude lower than the blocks intrinsic permeability. Lower values were not possible due to slow convergence. The porosity of the joint material was 0.01 for considering the joint material homogeneous and avoiding water accumulation. The water retention and the initial liquid pressure considered were the same the pellets material for avoiding numerical problems.

3.3.2 Mechanical parameters

The mechanical parameters can be divided between the strength and the stiffness parameters. The strength parameters were provided by SKB and were null cohesion and friction angle of 7.2° following the Mohr-Coulomb constitutive model. The zero-thickness elements followed the Mohr-Coulomb constitutive model and the parameters were the same. In joint element, the constitutive model was the Drucker-Prager and the equivalent parameter is $\delta = \frac{6sin\phi'}{3-sin\phi'}$, which value was 0.262. δ parameter is equivalent to M in Cam-clay model.

The assessment of the joint stiffness was done analysing the friction test results presented in Dueck et al. (2018), see Figure 3-5 and Figure 3-6.

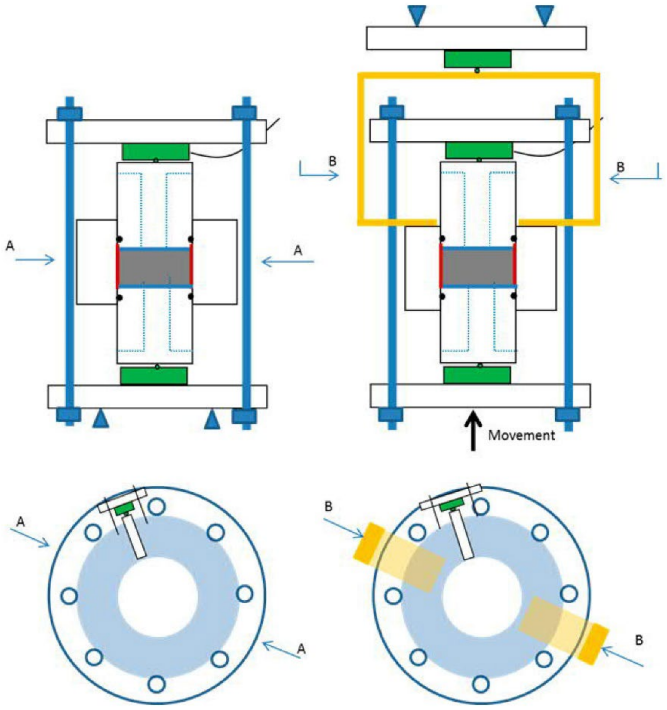

Figure 3-5. Friction test set-up (Appendix 2, Dueck et al. 2018).

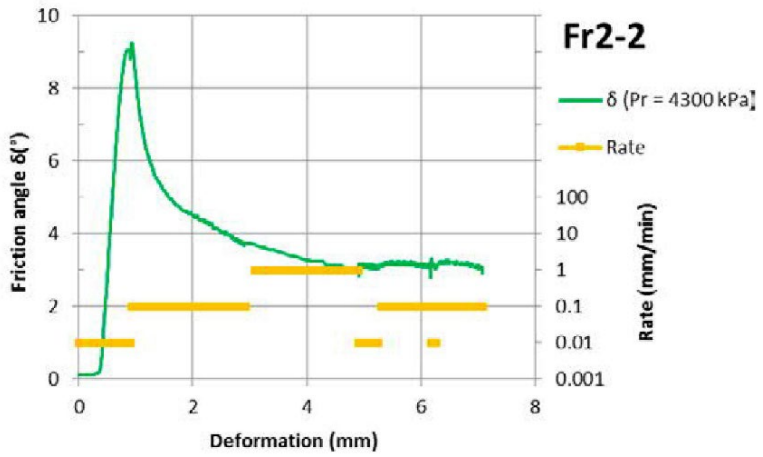

Figure 3-6. Friction test results when the swelling pressure was 4300 kPa (Appendix 2, Dueck et al. 2018).

Considering the shear stress τ as

$$\tau = tan\delta \times \sigma_n \tag{3-25}$$

Where δ is defined in Figure 3-6 (friction angle in this case) and σ_n is the axial stress.

k_s (shear stiffness) is defined as

$$\tau = k_s u \tag{3-26}$$

The value of k_s calculated was 1531 MPa/m (Figure 3-7). This parameter can be used in zero-thickness elements and as spring constant fixing the axial nodal force inside boundary as well. The relation between k_n and the aperture (a) and the minimum aperture (a_{min}) is

$$k_n = \frac{m}{a - a_{min}} \tag{3-27}$$

The k_n was 148123 MPa/m, considering a=0.025 m, a_{min}=0.001 m, m=3555 MPa. The large value of k_n does not allow radial displacements because the rock is considered stiff. Obviously, k_n is a value arbitrarily hight.

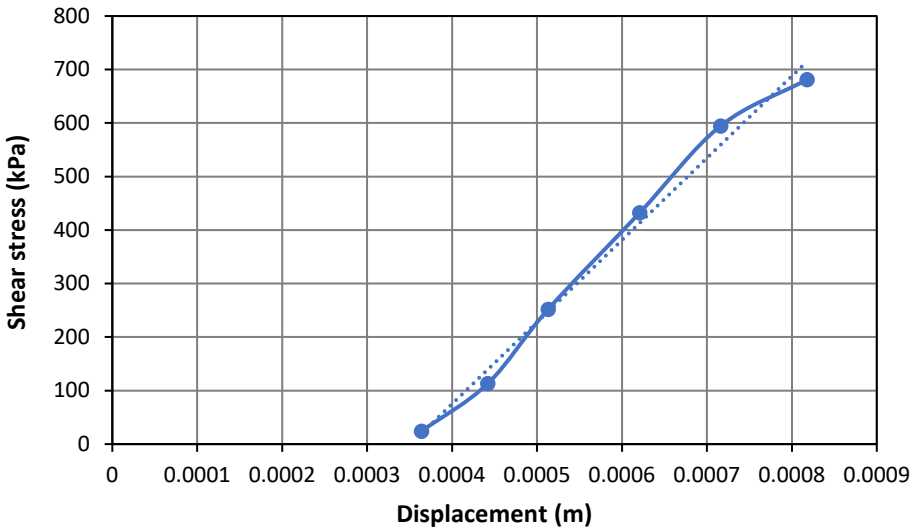

Figure 3-7. Shear stress vs shear displacement.

The joint material model needs the Young modulus and the Poisson ratio for defining the elastic part of the model. The Poisson ratio chosen was close to 0.5 in order to have a material without volumetric changes. The value chosen was 0.495. Values too close to 0.5 might cause numerical problems. The Young modulus chosen was the value which provided the shear modulus calculated from the test results with the equation

$$E = 2G(1 + \nu) \tag{3-28}$$

The calculation of G needs to fix a joint thickness. In this case, the thickness (L) chosen was 25 mm, which is an arbitrary value. The shear modulus can be calculated from the relation between the shear stress τ calculated following the equation (3-25) and the shear strain γ calculated as

$$\gamma = \frac{u}{L} \tag{3-29}$$

The relation τ–γ is presented in Figure 3-8. The value of the shear modulus obtained was 38.3 MPa and the Young modulus calculated from the equation (3-28) was 114.5 MPa.

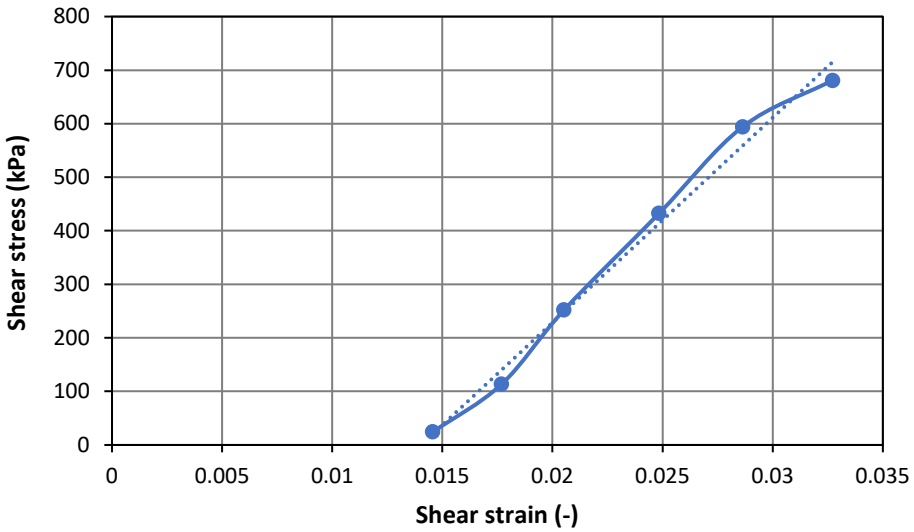

Figure 3-8. Shear stress vs shear strain.

More information regarding the friction can also be found in Sinnathamby et al. (2014) and in Dueck et al. (2016).

The mechanical parameters of the joint material are presented in Table 3-6 and the mechanical parameters of the zero-thickness elements in Table 3-7.

Table 3-6 Mechanical parameters of the joint material.

Parameter	Symbol	Value	ICL	ITYCL	Parameter
Young modulus (MPa)	E	114.5	1	1	P1
Poisson ratio (-)	ν	0.495	1	1	P3
Power of the stress function (-)	m	3	33	5	P1
Fluidity ($s^{-1}MPa^{-m}$)	Γ_0	10^{-5}	33	5	P2
Cohesion (MPa)	c	0	33	5	P5
Parameter to reduce dilatancy (-)	α	1	33	5	P7
Equivalent to *M* (critical state line) (-)	δ	0.262	33	5	P10

Table 3-7 Mechanical parameters of the zero-thickness elements.

Parameter	Symbol	Value	ICL	ITYCL	Parameter
Model parameter related with axial stiffness (MPa)	m	3555	1	16	P1
Shear stiffness (MPa/m)	K_s	1531	1	16	P2
Out of plane stiffness (MPa/m)	E	0.3555(1)	1	16	P3
Minimum aperture (m)	a_{min}	0.001	1	16	P4
Initial aperture of the joint (m)	a_0	0.025	1	16	P5
Cohesion (MPa)	c_0	0.001	34	16	P1
Friction angle (°)	ϕ	7.2	34	16	P2
Residual friction angle (°)	ϕ_{res}	7.2	34	16	P4
Critical value of shear displacement for cohesion (m)	u_c^*	0.015(2)	34	16	P5
Critical value of shear displacement for friction (m)	u_ϕ^*	0.015(2)	34	16	P6
Model parameter for dilatancy function (-)	χ_d	0(2)	34	16	P7
Model parameter for dilatancy function (-)	β_d	0(2)	34	16	P8
Joint asperity angle (°)	α_a	0(2)	34	16	P9
Compression strength for which dilatancy vanishes (MPa)	q_u	100(3)	34	16	P10
Fluidity ($s^{-1}MPa^{-m}$)	Γ_0	10^{-4}	35	16	P3
Power of the stress function	N	2	35	16	P4

(1) Lateral expansion of the joint allowed. This value does not have influence in the results of the current problem.

(2) Values from the example in CODE_BRIGHT tutorial. These values do not play any role due to there is not softening (ϕ=ϕ_{res}).

(3) Arbitrary value. Without dilatancy (χ_d=0), q_u does not play any role

If the boundary condition is fixed with springs at axial sense at the side boundary, the value of $\cos\beta_2$ is 3.9123×10^{-4}. This value is calculated using the equation 3-24 taking into account that f_y should be σ_y and that the value of γ is the default value (10^{10} MPa/m). With these values, the constant spring is the same as the K_s in zero-thickness elements ($10^{10}\times(3.9123\times10^{-4})^2$=1531 MPa/m).

4 Results

The results obtained are presented in this section. The simulations were run up 300 years, which was enough for finishing the 90% of the saturation process. The Base case was also run till 20000 years for checking the time needed for reaching the steady state conditions. When the water flow was only from the bottom of the deposition hole, the case was also run up 20000 years.

4.1 Base case

The Base case is a reference case and was run with a set of parameters defined from the previous references but also considering the relation swelling pressure – dry density presented in Section 3.1.

The Base case was used for studying the tolerances in calculations, the differences between the small strains setting and the updated mesh (Lagrangian option in CODE_BRIGHT), the thickness of the joint and the mesh dependency. The implementation of the friction was also analysed.

The joint model considered in the Base case was the approach with the viscoplastic model (joint material) presented in Section 3.3.

4.1.1 Geometry

The geometry was a simplified variant of a deposition hole in KBS-3V alternative, where the canister was not considered. The diameter of the deposition hole is 1750 mm with a pellet slot of 50 mm placed between the hole wall and the buffer blocks, which have a diameter of 1650 mm. The total height of the buffer is 8000 mm.

The simulations were carried out assuming axisymmetric symmetry.

4.1.2 Mesh

The mesh used had 6834 nodes and 6600 quadrilateral elements. The mesh was regular and the dimensions of each element was 27.5 mm width × 40 mm height. The element type used in CODE_BRIGHT was Type 5 (2-D). These elements are linear quadrilateral with selective integration by means the modification of the B matrix (Hughes 1980). This avoids locking when the medium is highly uncompressible (DECA-UPC 2021). Numerical integration with 4 points was applied.

4.1.3 Initial conditions

The Base case assumes a dry density of the buffer blocks of 1613 kg/m^3 and a dry density of pellets filling of 950 kg/m^3. If the density of solids considered is 2780 kg/m^3 (Åkesson et al. 2010, Pintado et al. 2018), the initial porosity and void ratio of buffer blocks are 0.420 and 0.723 and the initial porosity and void ratio of pellets filling are 0.658 and 1.93.

The initial porosity can be calculated following the equation:

$$e = \frac{\rho_{solids}}{\rho_d} - 1 \qquad (4\text{-}1)$$

4.1.4 Boundary conditions

The simulations performed were hydro-mechanical, so hydraulic and mechanical boundary conditions must be defined.

Hydraulic boundary conditions

The hydration in the Base case was through the side surface (see Figure 2-1). The upper boundary remained impervious (backfill did not supply water to the buffer).

Mechanical boundary conditions

The axial displacements were not allowed at the bottom and neither the radial displacements nor the axial displacements were allowed at the side. This means that buffer could swell in radial sense at the bottom, without rock friction. The consideration or not of friction at the bottom does not have any influence at the results. The side boundary was fixed, so the rock did not move. The axial movements in buffer – rock interface were function of the joint material considered.

4.1.5 Sensitivity analysis in Base case

A sensitivity analysis was performed in the Base case for studying the dependency on tolerances, mesh size, joint properties and joint thickness and the also for deciding how to implement the friction in rock wall. The variable compared is the axial displacements in buffer – backfill contact (Figure 4-1).

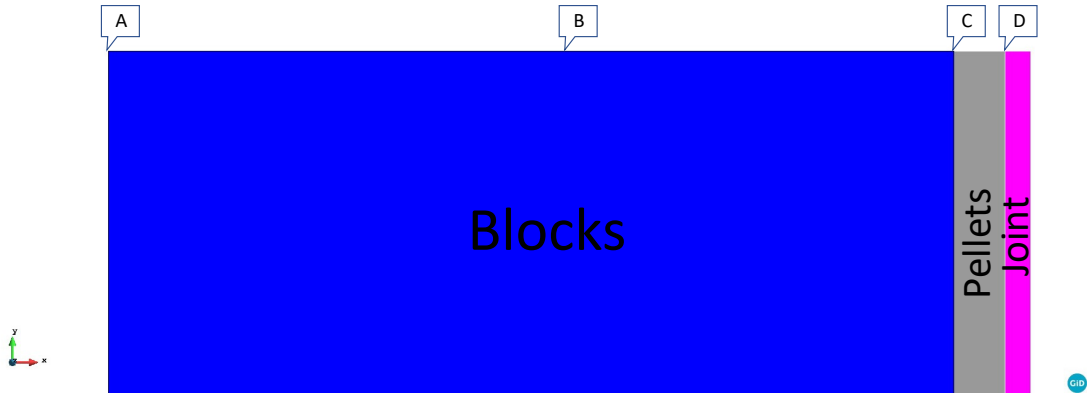

Figure 4-1. Differences in axial displacements as function of the tolerances.

Tolerances

The tolerance in displacements was 10^{-6} m and in liquid pressure was 10^{-2} MPa. The displacement tolerance was reduced till 10^{-8} m and the liquid pressure till 10^{-3} MPa but it was not possible to reach convergence, then, the tolerances were fixed at 10^{-7} m and 5×10^{-2} MPa. The differences in vertical displacements in axis and in buffer – contact were negligible in buffer – joint contact (Figure 4-2).

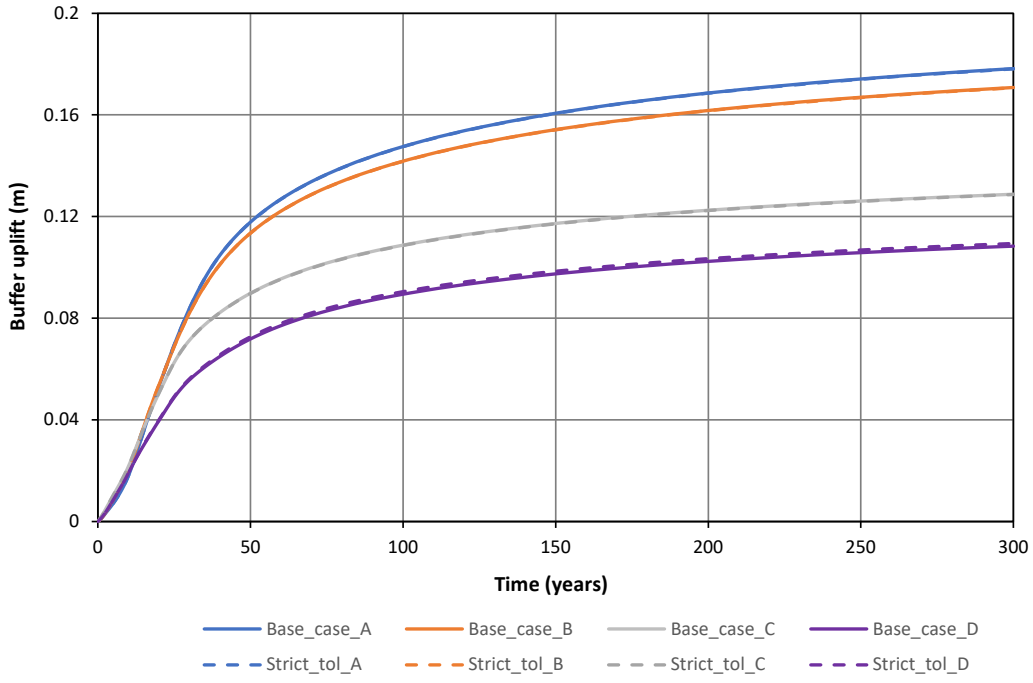

Figure 4-2. Differences in axial displacements as function of the tolerances.

Mesh size

The elements size was reduced till have a mesh with 29273 nodes and 28800 elements. The vertical displacements in some upper boundary nodes were compared with the reference mesh and the differences were negligible in points A, B and C and small in point D (Figure 4-3).

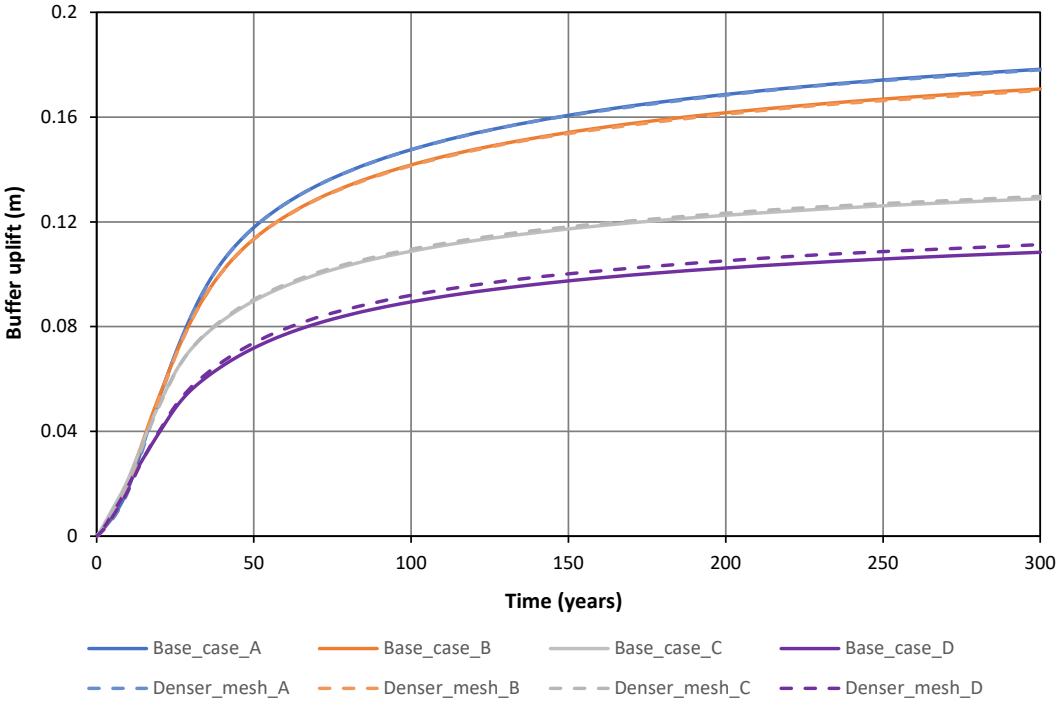

Figure 4-3. Differences in axial displacements as function of the mesh size.

Joint Viscosity

The joint constitutive model was viscoplastic, this means that there is a certain dependency on the time if the viscosity is large and the viscoplastic model converges to a plastic model when the viscosity is small enough for avoiding dependency on time. When the viscosity was small (in CODE_BRIGHT, the viscosity is related with the "fluidity", inverse of the viscosity), it was not possible to reach convergence. The fluidity was decreased (increasing the viscosity) and it was possible to reach convergence. Two extreme values are compared in Figure 4-4, where the Base case was run with a fluidity value of 10^{-5} $s^{-1}MPa^{-3}$ and the largest value with convergence was 0.1. The differences were negligible in points A, B and C and small in point D.

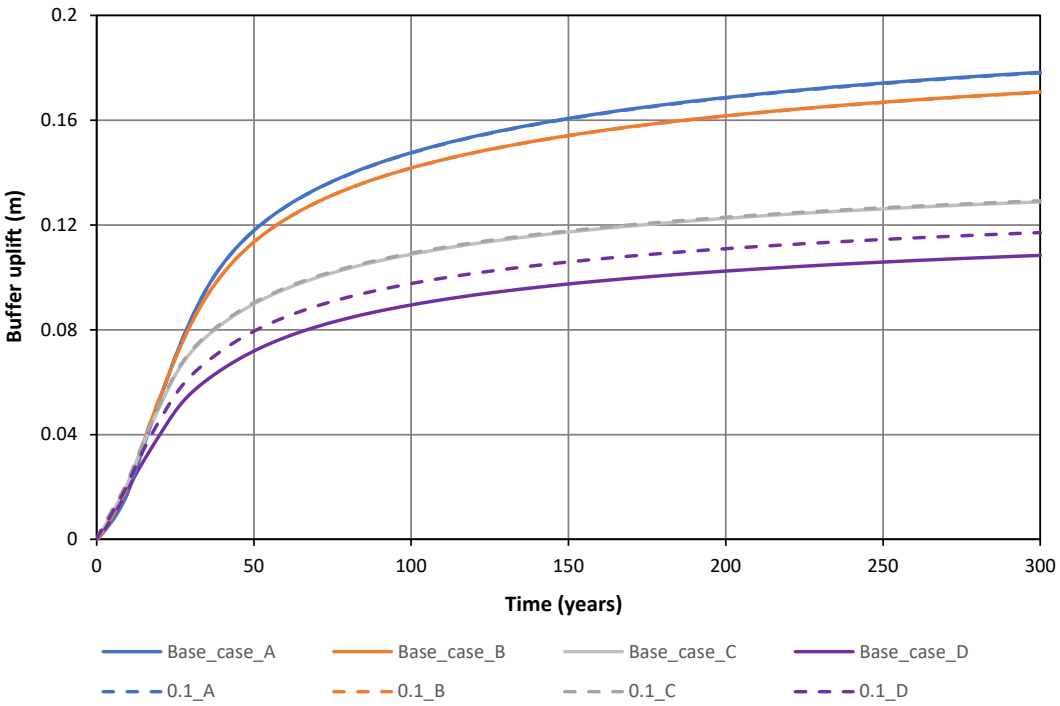

Figure 4-4. Differences in axial displacements as function of the joint viscosity.

The buffer upwards of point D as function of the fluidity is presented in Figure 4-5. The value remains quite stable, a bit more than 0.1 m. The differences were probably due to the tolerances.

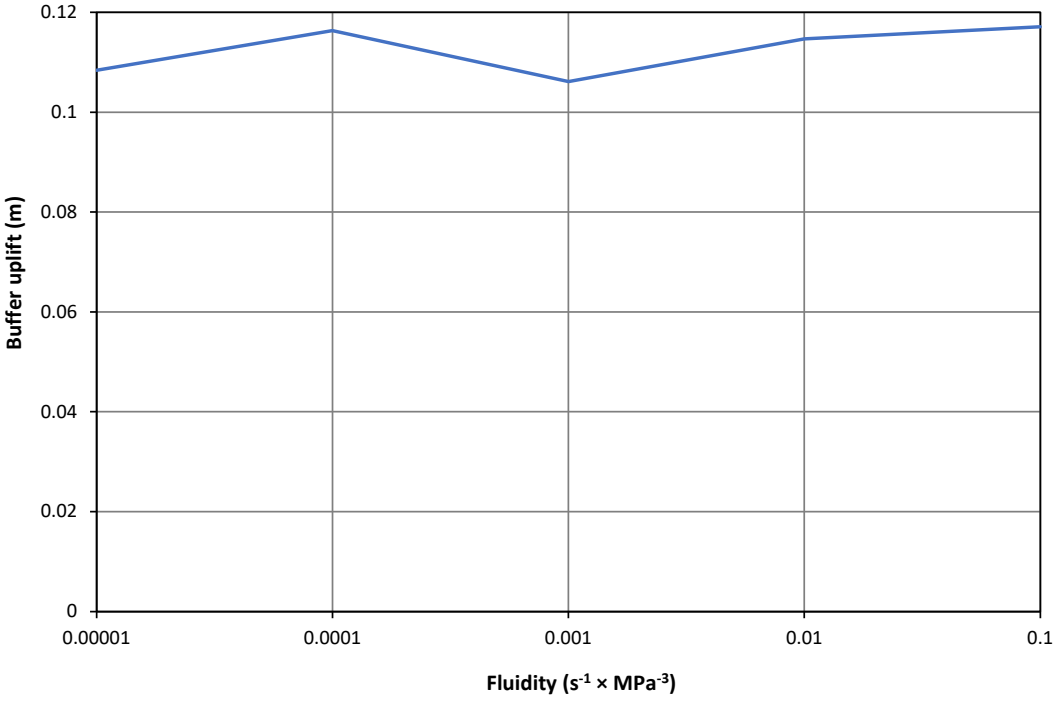

Figure 4-5. Differences in axial displacements as function of the joint viscosity.

Joint thickness

The joint thickness was reduced from 0.025 m to 0.005 m and the shear modulus increased five times. Figure 4-6 shows the differences in point A, B and C (negligible) and in D.

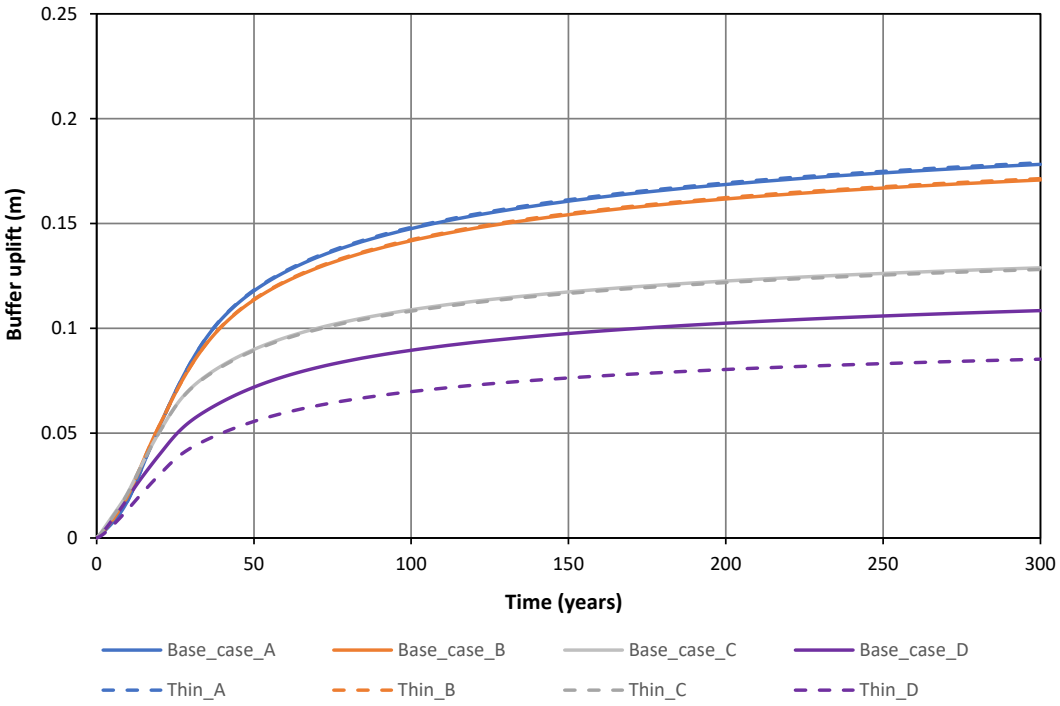

Figure 4-6. Differences in axial displacements as function of the joint thickness.

Updated Lagrangian setting

The Base case was run with the small strains setting. Due to the large strains expected in the upper part of the buffer, the Base case was used to check the small strains simulation against the updated Lagrangian simulation implemented in CODE_BRIGHT. The updated Lagrangian is an approximation to large strains setting which can work correctly if there are not rotations. The Lagrangian option did not converge when the time reached 16 years. The tendency during the convergence period showed similar results in both settings (Figure 4-7) but due to the short period of time, it is not possible to conclude anything.

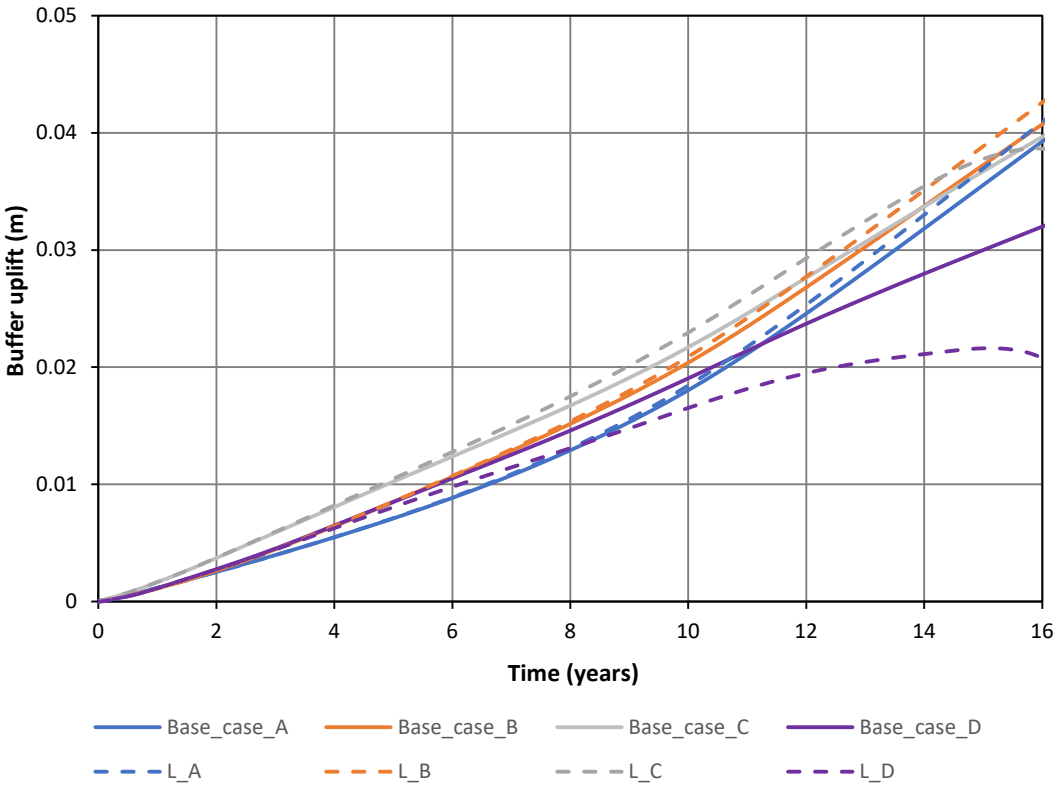

Figure 4-7. Differences in axial displacements in Lagrangian and small strains settings.

Alcoverro and Pintado (2021) carried out an analysis comparing the small strains with the large strain settings implemented in PLAXIS computer code. It is possible to assess the difference between the small strains analysis and the large strains analyses but taking into account that there are many rates for considering the large strains. PLAXIS has implemented the Hill rate (van Langen 1991). This rate is equivalent to Jaumann rate, implemented in Abaqus computer code, if there are not volumetric changes.

There are two regions of the buffer where it can be expected large strains. The first one is the contact buffer – rock, where large shear strains can be expected, especially at the buffer – backfill contact. The behaviour of this contact is close to the behaviour of a simple shear test (Figure 4-8).

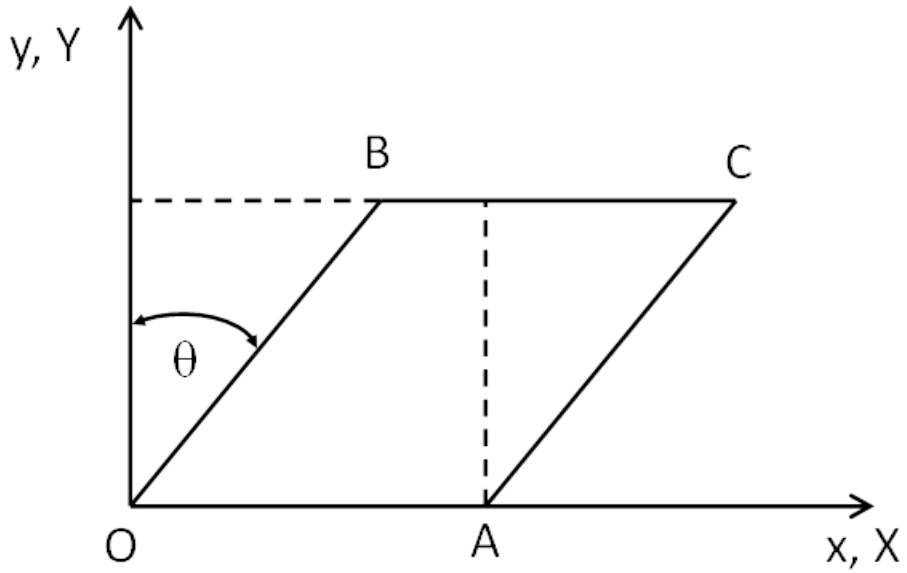

Figure 4-8. Simple shear test diagram.

The value of θ can be calculated from the results presented in Figure 4-12. If it is considered a simple shear test performed in a material with a Young modulus of 114.5 MPa and Poisson ratio of 0.495 (see Table 3-6), equivalent to a shear modulus of 38.294 MPa, in a sample with 0.025 m height, it is possible to obtain the solution of the simple shear test taking into account the small strains and the Jaumann rate in large strains setting.

The results are presented in Figure 4-9. It is possible to see the oscillation of the Jaumann solution, which is a well-known problem. The scope of this discussion is just to check when the small strain hypothesis starts to diverge respect the results obtained when the large strains formulation is used. It is important to point out that there are many large strains formulations, as a matter of fact, there could be infinite, and the results with another formulation might be different.

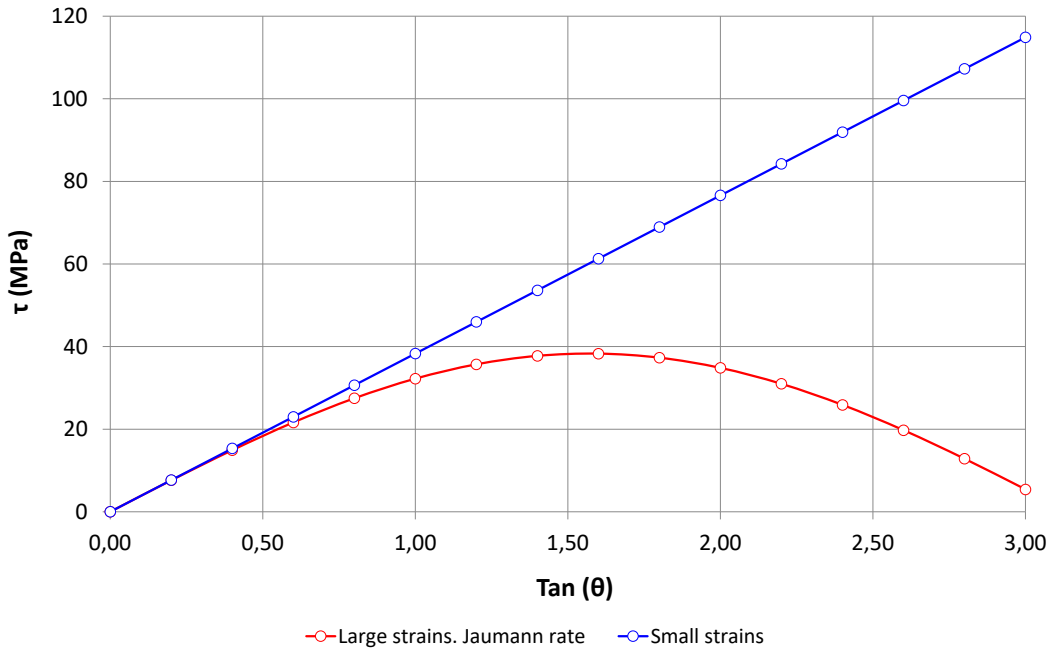

Figure 4-9. Simple shear test results.

Table 4-1 show the values of tan(θ) calculated from the simulation of the Base case. At 0.08 m of the buffer – backfill contact, the value of the tan(θ) is almost 1, at this value, the small strains and the Jaumann large strains setting present similar results, so it is possible to conclude that the large strains are necessary only at the first 10 cm from the contact buffer – backfill.

Table 4-1 Uplift and Tan(θ) values in buffer – rock contact.

Distance to the buffer – backfill contact (m)	Uplift (m)	Tan (θ)
0	0.108	4.34
0.04	0.0455	1.82
0.08	0.0260	0.984
0.12	0.0125	0.498
0.16	0.00914	0.365
0.2	0.00699	0.280

The second region where the effect of the large strains might have influence in the results is the axis of the deposition hole, where the highest axial displacements are expected. The buffer might behave as an oedometer but only if the water flow comes only from the bottom. Due to the flow is radial and axial, the behaviour is not like an oedometer at the entire buffer but near the axis of the deposition hole, the radial displacements are the smallest and the axial the largest, so the behaviour might be considered oedometric (Figure 4-10).

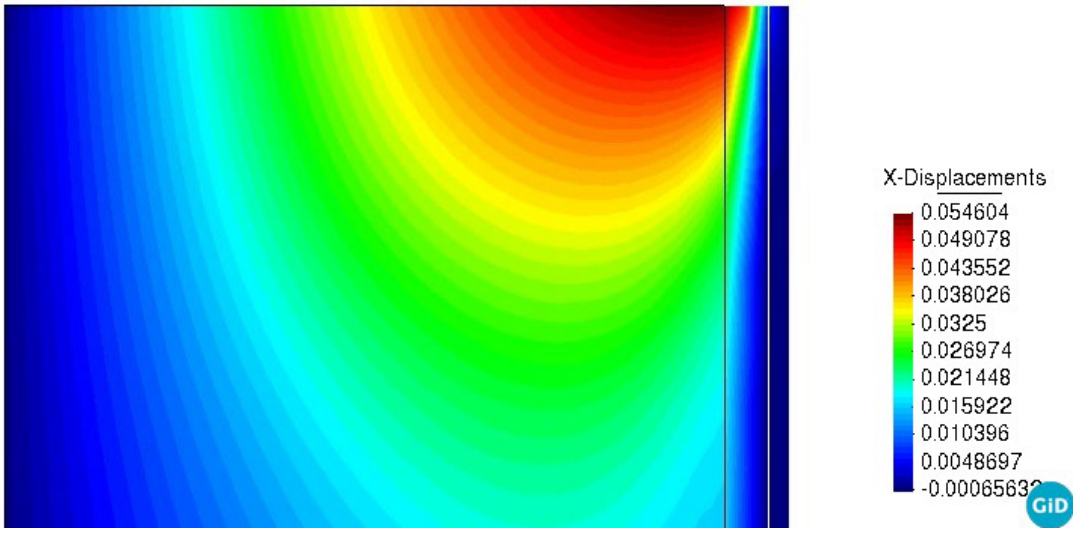

Figure 4-10. Radial displacements (X-Displacements) in Base case after 300 years.

The Appendix 1 presents a study of the oedometer test with different settings. It is possible to see that the small strains setting is mathematically identical to the large strains setting considering the Truesdall rate. The updated Lagrangian setting available in CODE_BRIGHT is mathematically identical to the large strains setting considering the Jaumann rate. The kinematics effects in oedometric conditions can be considered with the both options available in CODE_BRIGHT without formal errors although as it can be seen in the Appendix 1, the results are different depending on the rate chosen for dealing with the large strains.

Implementation of the friction

The axial displacements as function of the joint model are presented in Figure 4-11a and Figure 4-11b, where the Base case implements the friction with a continuum joint material. The maximum displacement (point A) is similar in all cases but there are differences in the rest of the

points which increases when the point is closer to the rock. The case without relative displacement between rock and buffer (fix) is also presented.

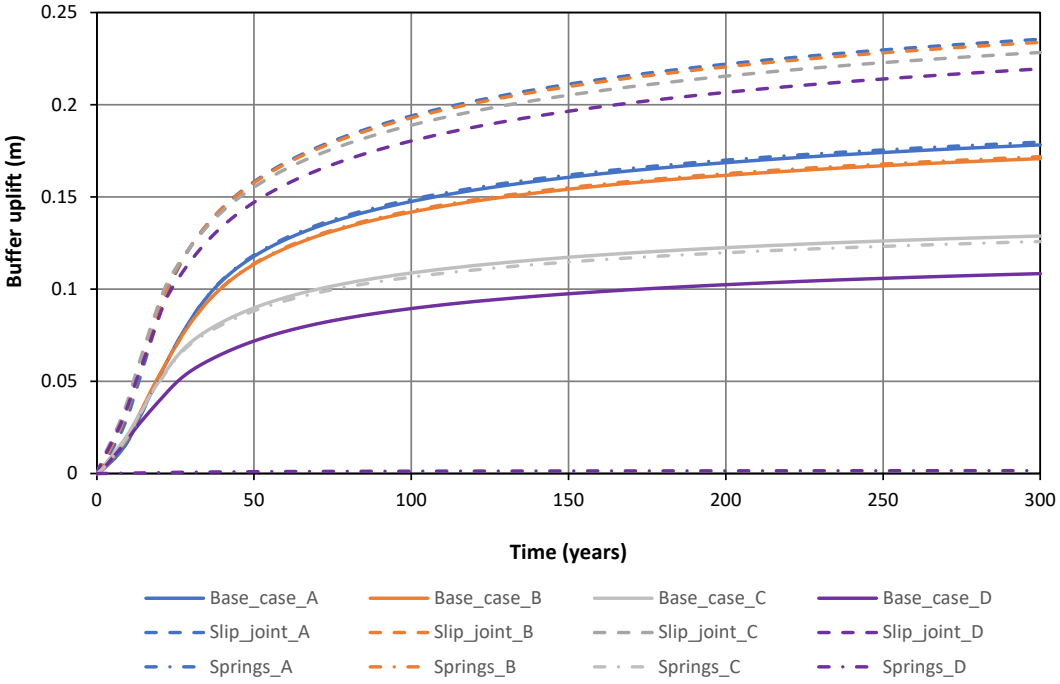

Figure 4-11a. Differences in axial displacements on top of the buffer as function of the joint model.

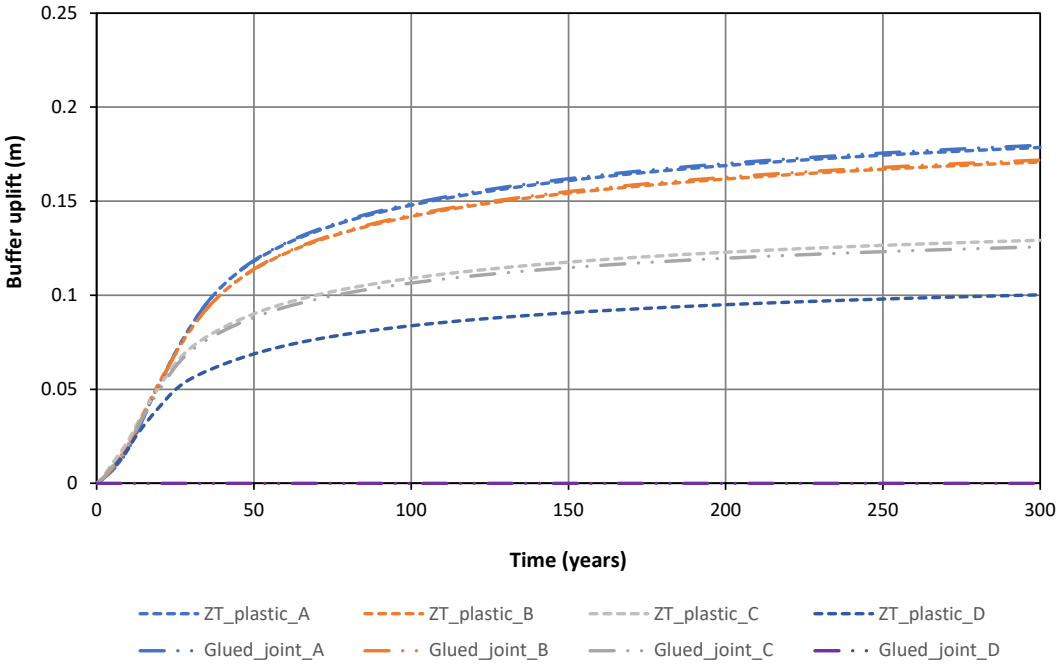

Figure 4-11b. Differences in axial displacements on top of the buffer as function of the joint model. ZT_plastic_D point cannot be represented due to a post-process issue. Note that the point D in glued joint does not move.

Figure 4-12 presents the axial displacements in buffer – rock contact as function of the joint model. It is possible to see that the joint material and zero-thickness elements gave similar results, with small differences on top due to the plasticity of the zero-thickness elements.

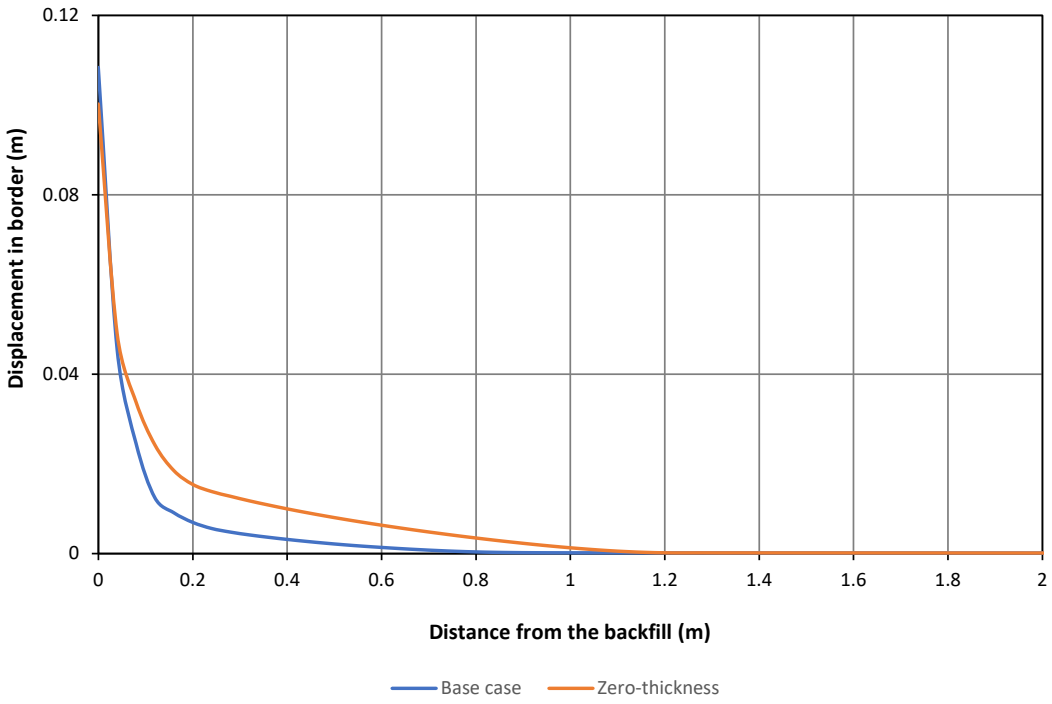

Figure 4-12. Y-displacements in pellets – rock contact as function of the joint model. Simulation time: 300 years. Plastic constitutive models.

Figure 4-13 shows the axial displacements in buffer – rock contact as function of the joint model for studying the different modelling options of the buffer – rock contact. The elastic options present certain instabilities, which are quite large when the zero-thickness elastic option is used and minimum when the joint elastic model is used. The zero-thickness in plasticity shows a small instability when the joint is close to plasticity as well. All models present the same results in the elastic part. The differences between joint model and zero-thickness model are due differences in the constitutive models considered.

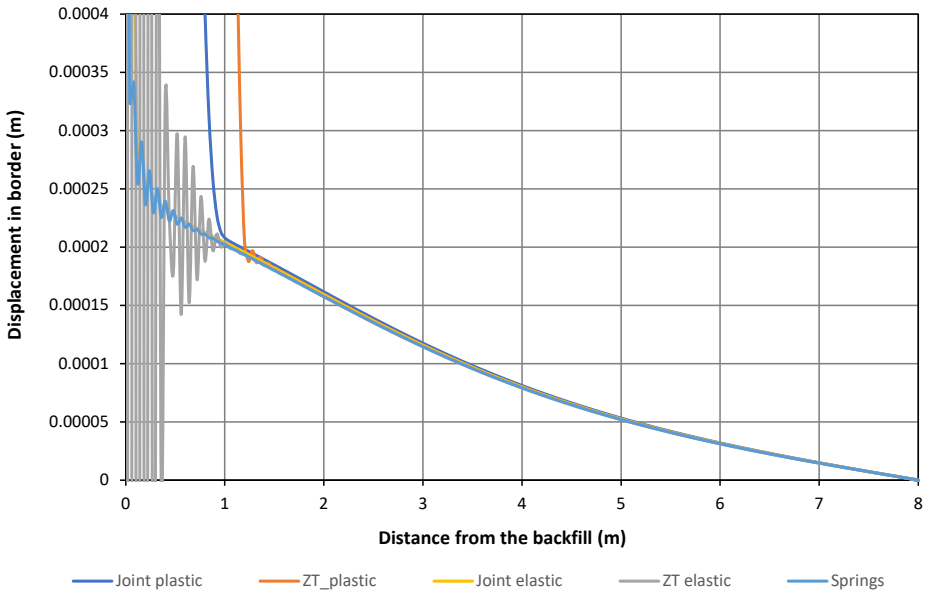

Figure 4-13. Y-displacements in pellets – rock contact as function of the joint model. Simulation time: 300 years. All constitutive models.

4.2 Sensitivity analysis

The sensitivity analysis was performed with the variation of the boundary conditions (Part 1) and the friction angle in two of the cases where the boundary conditions were analyzed (Part 2). The boundary condition is changed on top of the geometry in Case 1 (constant axial pressure) and Case 2 (softer springs). Hydraulic boundary condition is changed in Case 3, where the hydration is performed from the bottom (Figure 4-14). The initial blocks dry density, directly related with the porosity, is changed in Case 4 (smaller) and Case 5 (larger). Finally, the initial water content is changed in Case 6, where the initial conditions in blocks and pellets is fully saturation. Table 4-2 shows the summary of these cases.

Table 4-2 Cases to model. Part 1 (sensitivity analysis to boundary conditions).

	Base case	**Case 1**	**Case 2**	**Case 3**	**Case 4**	**Case 5**	**Case 6**
Axial pressure	Spring load k=20 MPa/m	Constant 1.5 MPa	Spring load k=750 kPa/m	Spring load k=20 MPa/m	Spring load k=20 MPa/m	Spring load k=20 MPa/m	Spring load k=20 MPa/m
Wetting	Side boundary	Side boundary	Side boundary	Bottom boundary	Side boundary	Side boundary	Bottom boundary
Blocks dry density	1613 kg/m^3	1613 kg/m^3	1613 kg/m^3	1613 kg/m^3	1479 kg/m^3	1670 kg/m^3	1613 kg/m^3
Water content	17%	17%	17%	17%	17%	17%	Saturated

Two cases (Base case and Case 2) were chosen for performing the sensitivity analysis to buffer – rock friction angle. Cases 7 and 8 had the Base case conditions but with friction angles of 1° and 5° and cases 9 and 10 had the Case 2 conditions but with friction angles of 1° and 5° as well. Table 4-3 shows the summary of the cases changing the friction angle.

Table 4-3 Cases to model. Part 2 (sensitivity analysis to buffer – rock friction).

	Case 7	**Case 8**	**Case 9**	**Case 10**
Axial pressure	Spring load k=20 MPa/m	Spring load k=20 MPa/m	Spring load k=750 kPa/m	Spring load k=750 kPa/m
Wetting	Side boundary	Side boundary	Side boundary	Side boundary
Blocks dry density	1613 kg/m^3	1613 kg/m^3	1613 kg/m^3	1613 kg/m^3
Water content	17%	17%	17%	17%
Friction angle	1°	5°	1°	5°

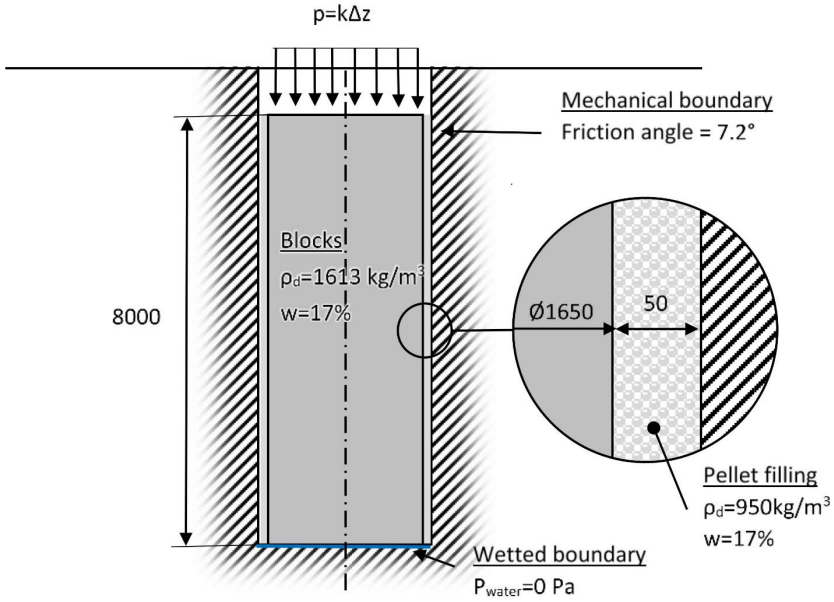

Figure 4-14. Illustration of wetting at the bottom.

The Case 6 was not run due to the initial conditions are equilibrium. This means that there is no water uptake as the liquid pressure is in equilibrium in all points of the geometry.

The initial conditions of the models were calculated taking into account the initial dry density and the initial water content presented in Table 4-2. The degree of saturation was calculated as:

$$S_r = \frac{{}^{w}/_{\rho_w}}{{}^{1}/_{\rho_d} - {}^{1}/_{\rho_{solid}}} \quad (4\text{-}2)$$

The initial conditions are presented in Table 4-4.

Table 4-4 Initial conditions.

	Base case	Case 1	Case 2	Case 3	Case 4	Case 5
Initial suction (MPa)	35.8	35.8	35.8	35.8	40.7	35.3
Initial porosity (-)	0.420	0.420	0.420	0.420	0.468	0.399
Initial degree of saturation (%)	65.3	65.3	65.3	65.3	53.7	71.1
Initial void ratio (-)	0.723	0.723	0.723	0.723	0.880	0.665

The buffer upwards calculated in the Base case and cases 1 and 2 (different boundary conditions in buffer – backfill interaction), the Base case and Case 3 (different inflow conditions) and the Base case and cases 4 and 5 (different initial dry densities) can be seen in Figure 4-15, Figure 4-16 and Figure 4-17.

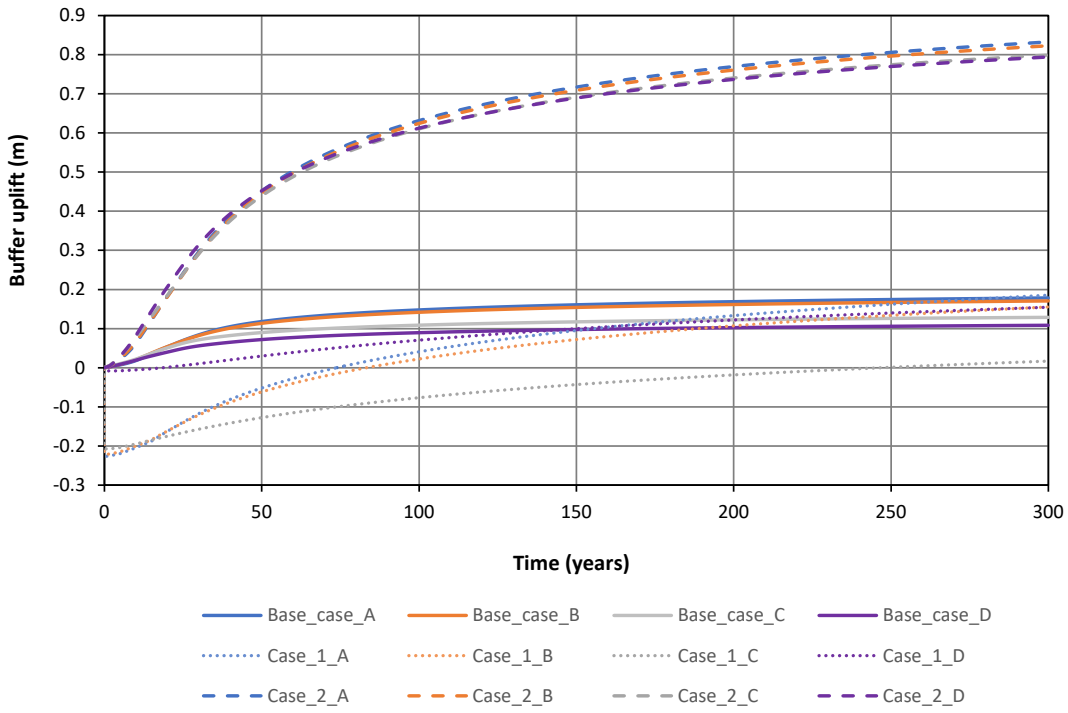

Figure 4-15. Buffer upwards at different buffer – backfill conditions.

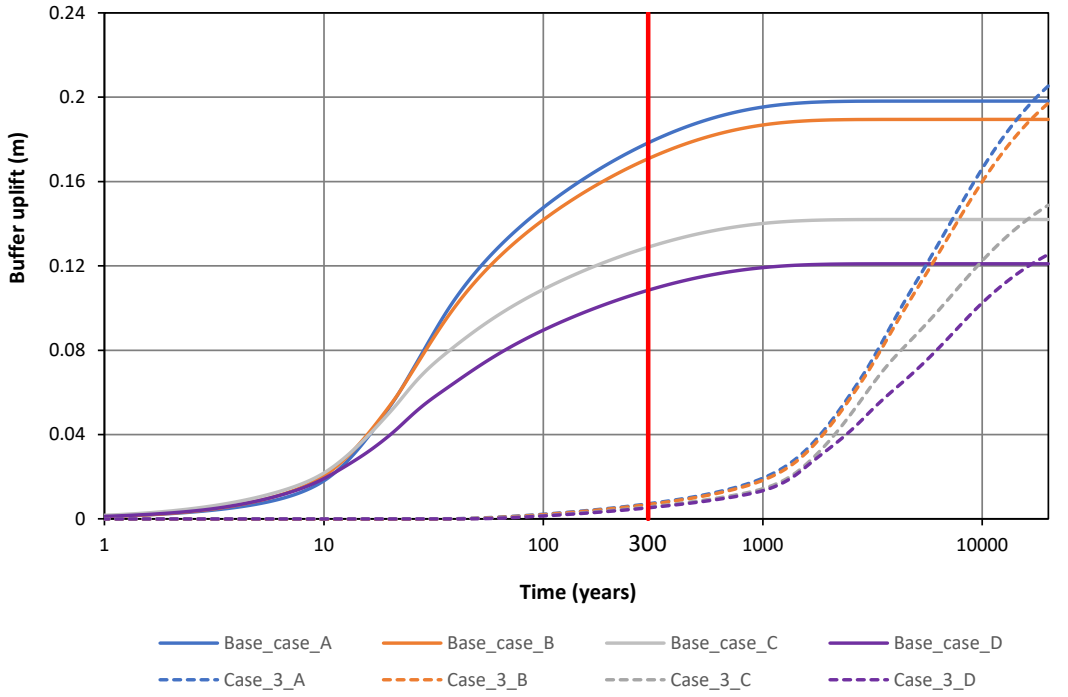

Figure 4-16. Buffer upwards at different inflow conditions. The Base case has been extended till 20000 years as well.

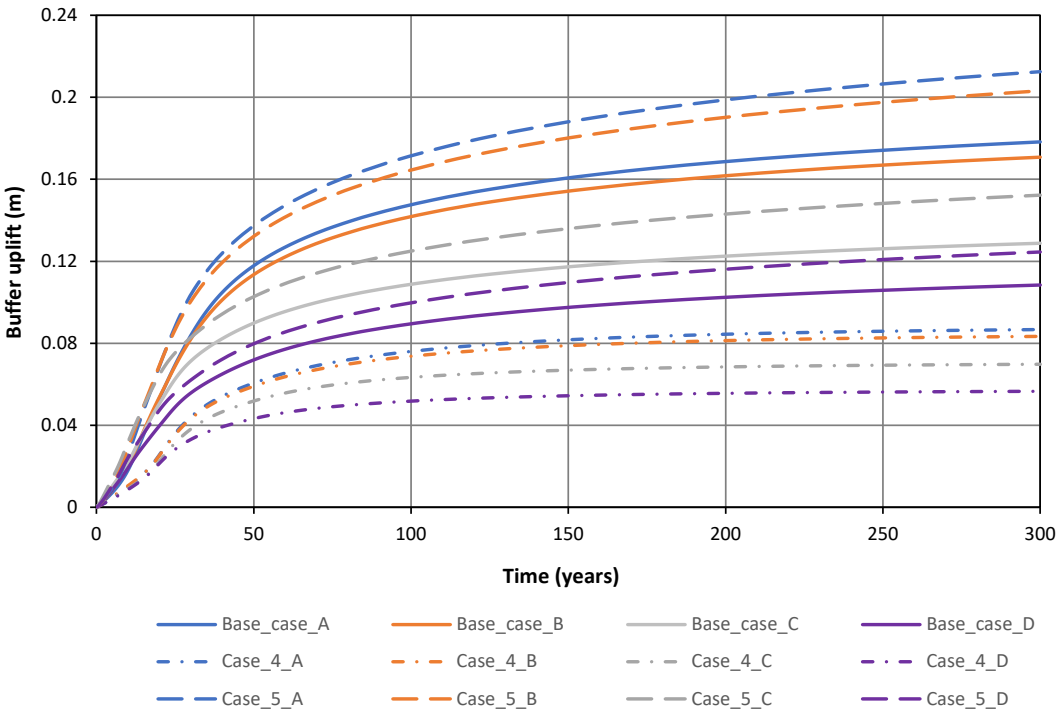

Figure 4-17. Buffer upwards at different initial dry densities.

The buffer upwards results as function of the friction angle are presented in Figure 4-18 (cases 7 and 8, Base case sensitivity analysis) and in Figure 4-19 (Cases 9 and 10, Case 2 sensitivity analysis). Note that points A and B follow the same behaviour in Base case and Case 8.

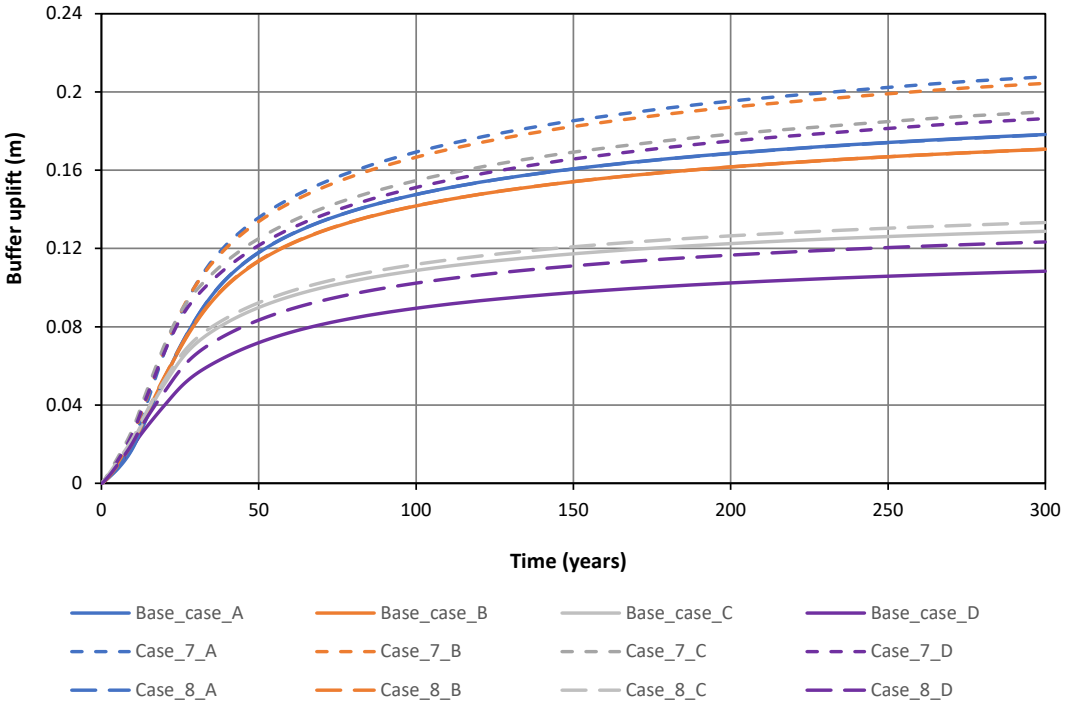

Figure 4-18. Buffer upwards with different friction angles (7.2° in Base case, 1° in Case 7 and 5° in Case 8). Points A and B follow the same behaviour in Base case and Case 8.

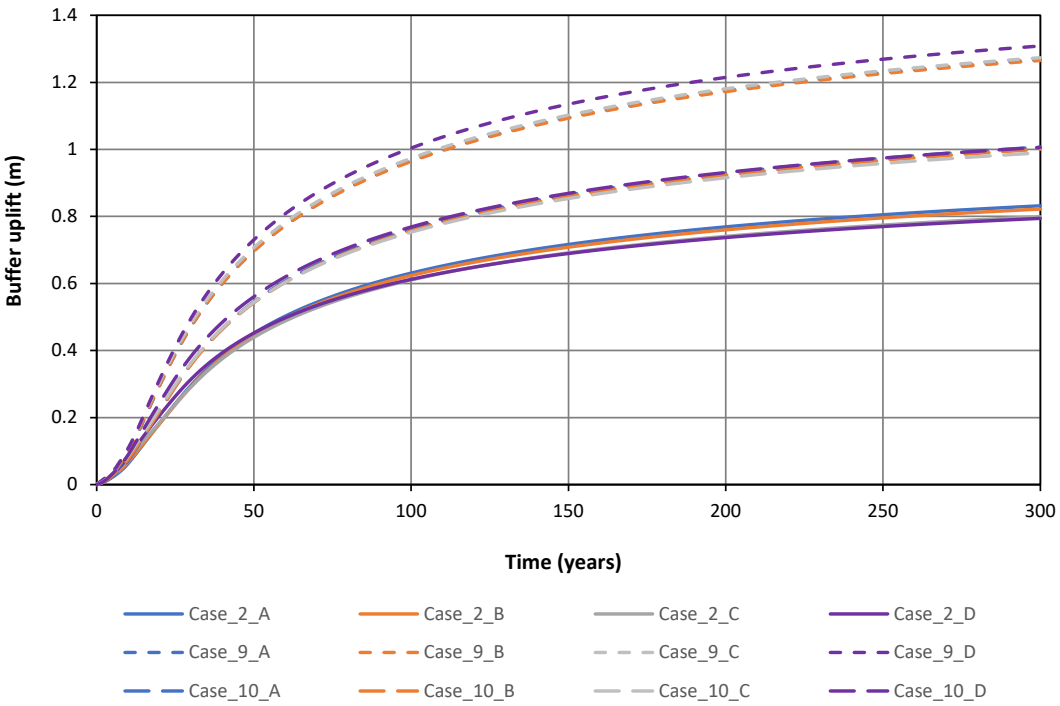

Figure 4-19. Buffer upwards with different friction angles (7.2° in Case 2, 1° in Case 9 and 5° in Case 10).

The zero-thickness element was analyzed with friction angles of 1° and 5° (Figure 4-20). As it could be expected, the lower friction angle the larger plastic domain.

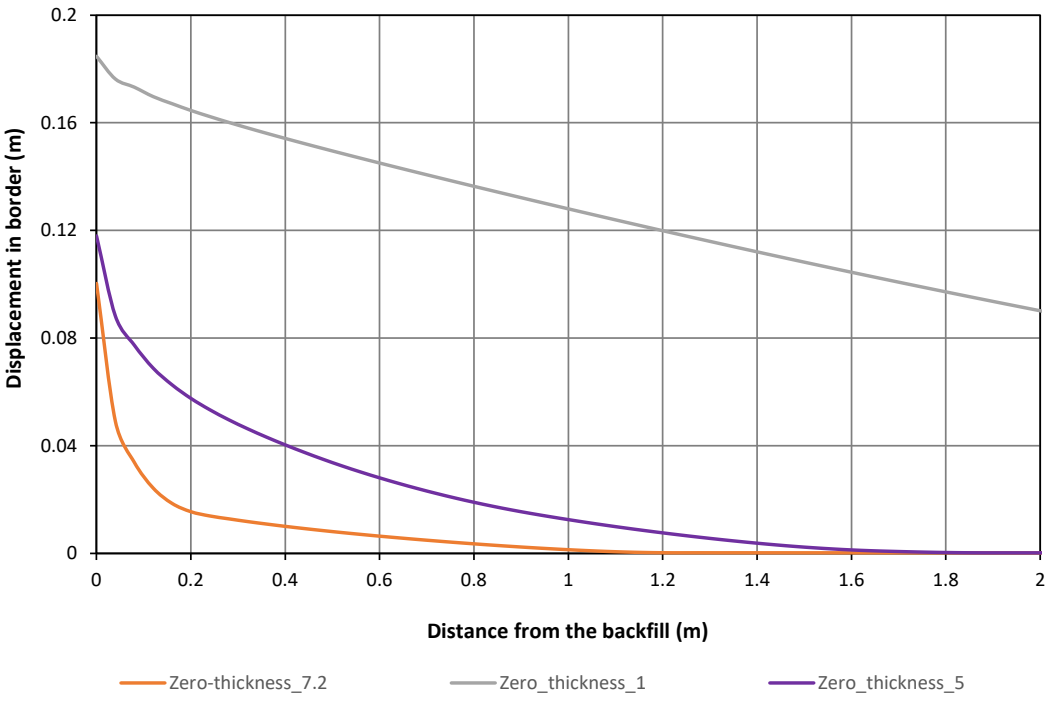

Figure 4-20. Y-displacements in pellets – rock contact as function of the friction angle in zero-thickness elements.

The buffer upwards and the swelling pressure developed at the axisymmetric axis are presented in Table 4-5.

Table 4-5 Buffer upwards and swelling pressure at the axisymmetric axis.

	Buffer upwards (m)	Swelling pressure (MPa)
Base case (k=20 MPa/m)	0.178	3.52
Case 1 (p=1.5 kPa)	0.185	1.53
Case 2 (k=0.75 MPa/m)	0.832	0.640
Case 3 (wetting from bottom)	0.205	4.17
Case 4 (low block dry density)	0.0867	1.76
Case 5 (high block dry density)	0.213	4.32
Case 7 (k=20 MPa/m and friction=1°)	0.208	4.17
Case 8 (k=20 MPa/m and friction=5°)	0.178	3.61
Case 9 (k=0.75 MPa/m and friction=1°)	1.27	0.928
Case 10 (k=0.75 MPa/m and friction=5°)	1.01	0.758

The dry density and the dry density distribution at the axisymmetric axis are presented from Figure 4-21 to Figure 4-30.

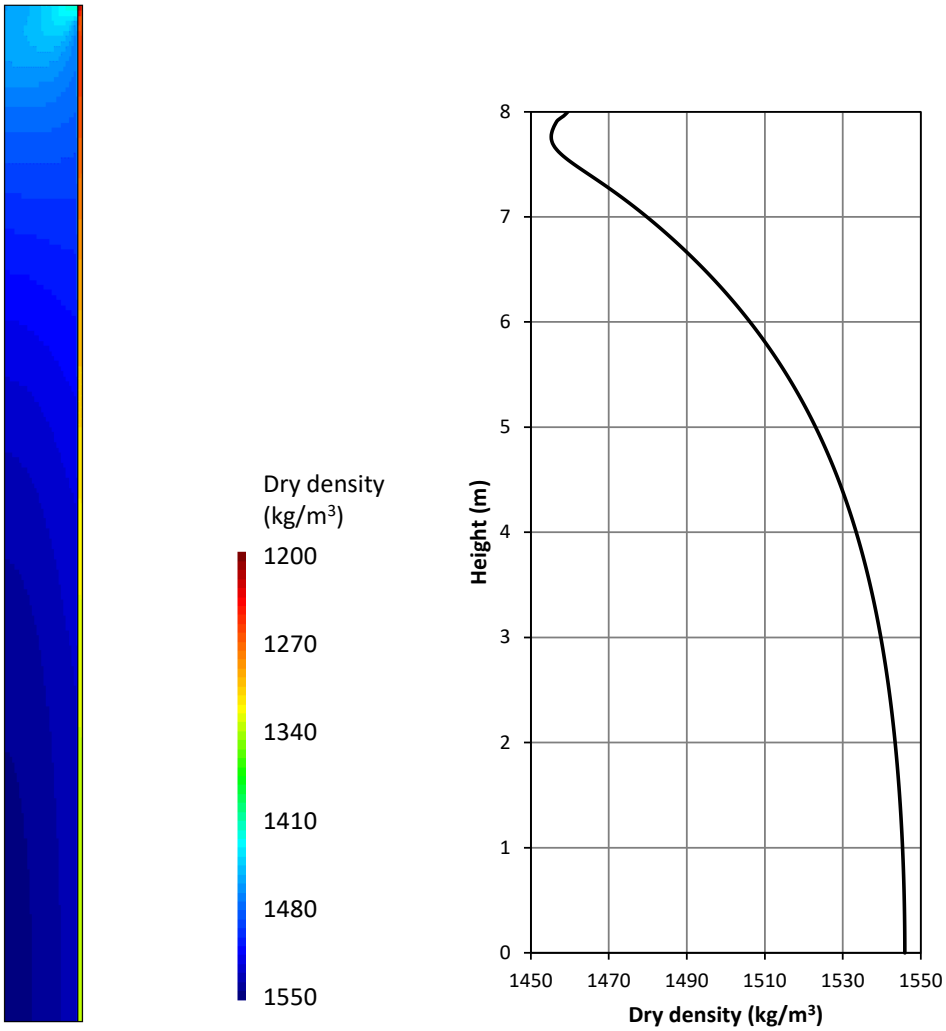

Figure 4-21. Dry density after 300 years (left). Dry density distribution at the axis after 300 years (right). Base case.

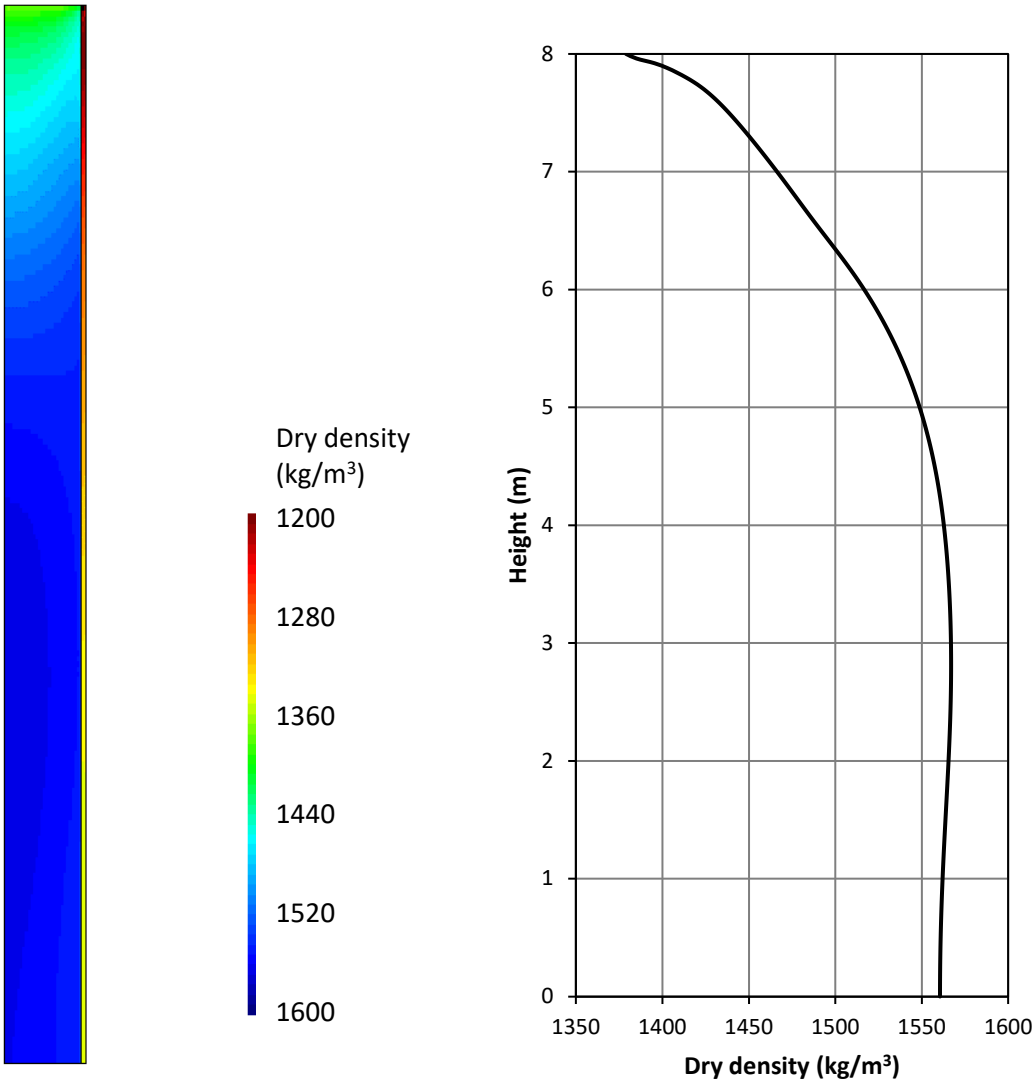

Figure 4-22. Dry density after 300 years (left). Dry density distribution at the axis after 300 years (right). Case 1.

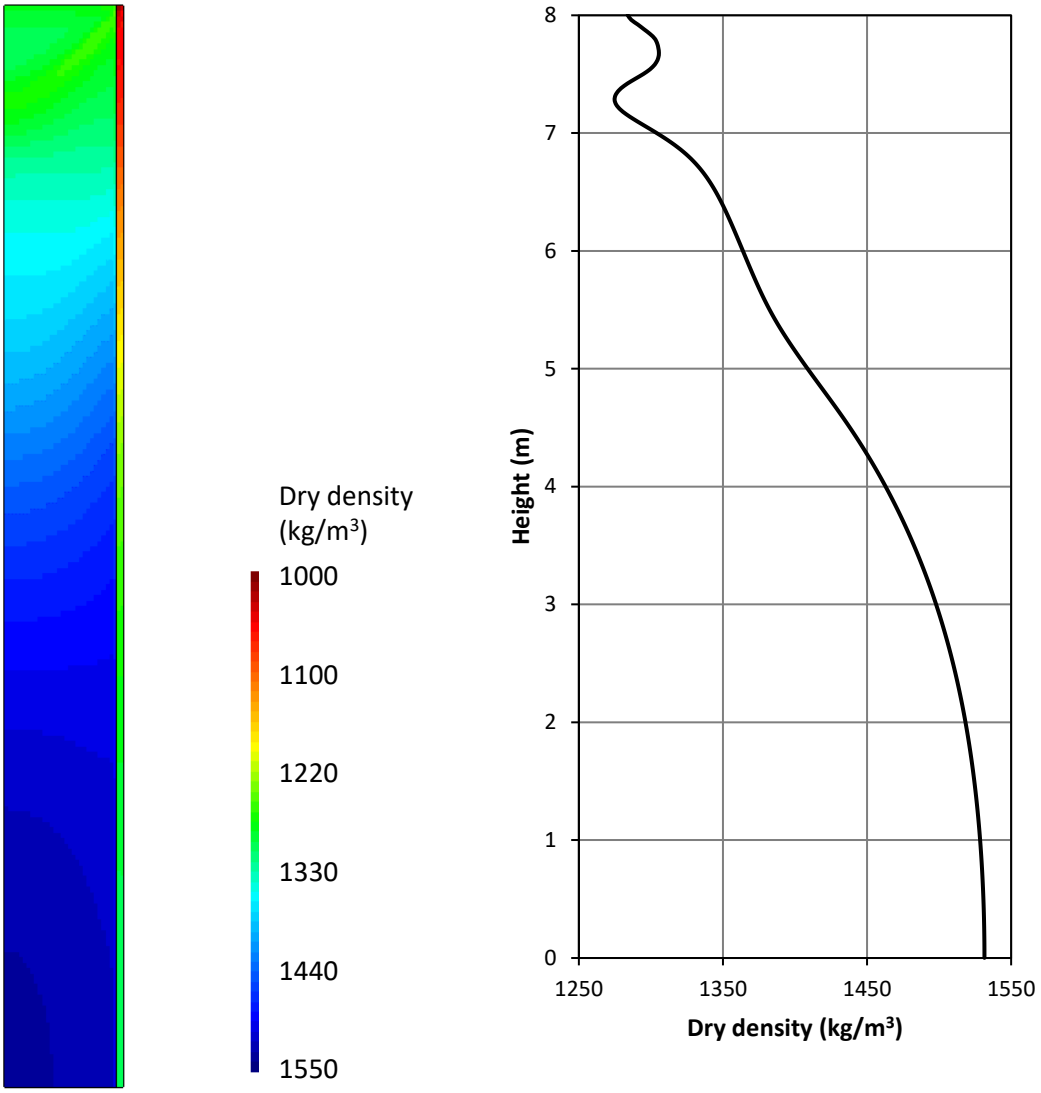

Figure 4-23. Dry density after 300 years (left). Dry density distribution at the axis after 300 years (right). Case 2.

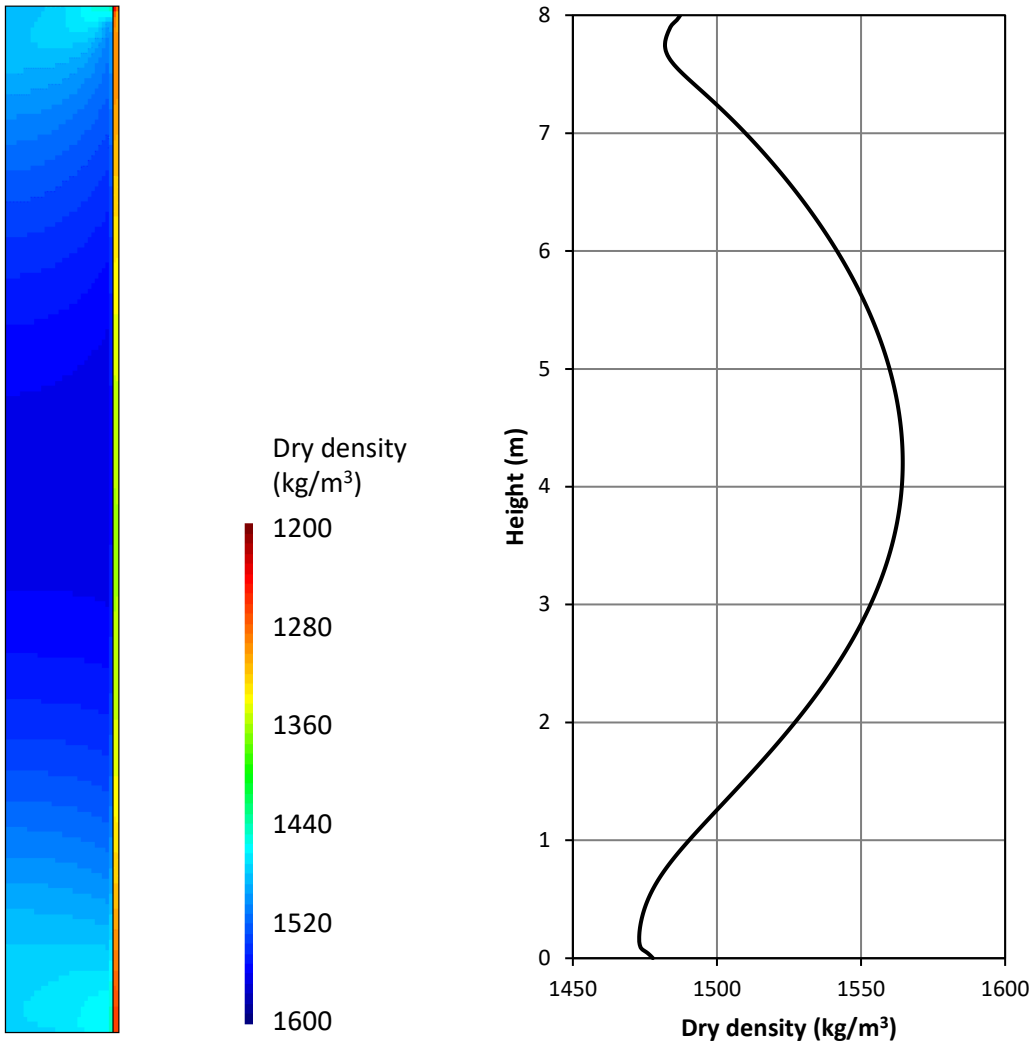

Figure 4-24. Dry density after 300 years (left). Dry density distribution at the axis after 20000 years (right). Case 3.

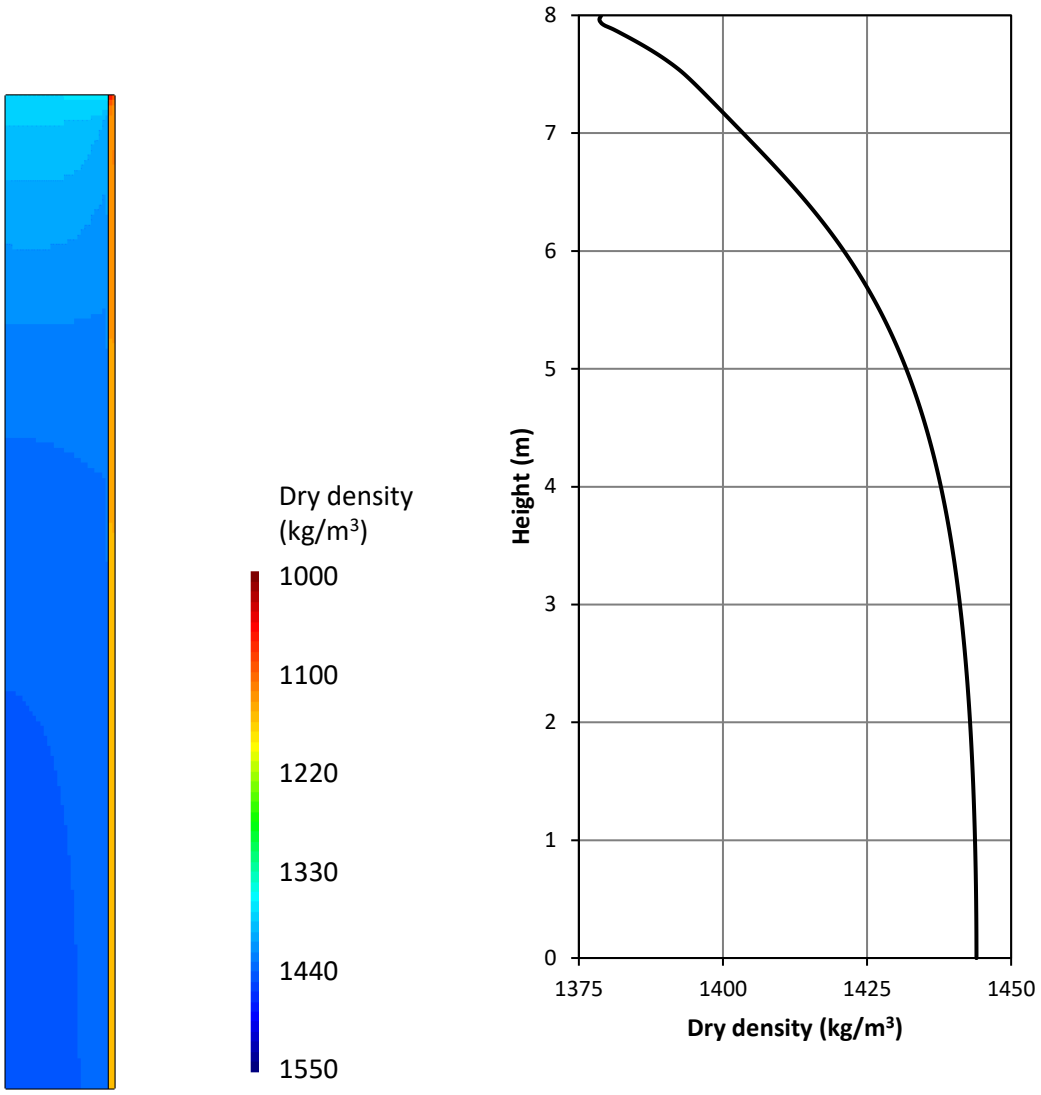

Figure 4-25. Dry density after 300 years (left). Dry density distribution at the axis after 300 years (right). Case 4.

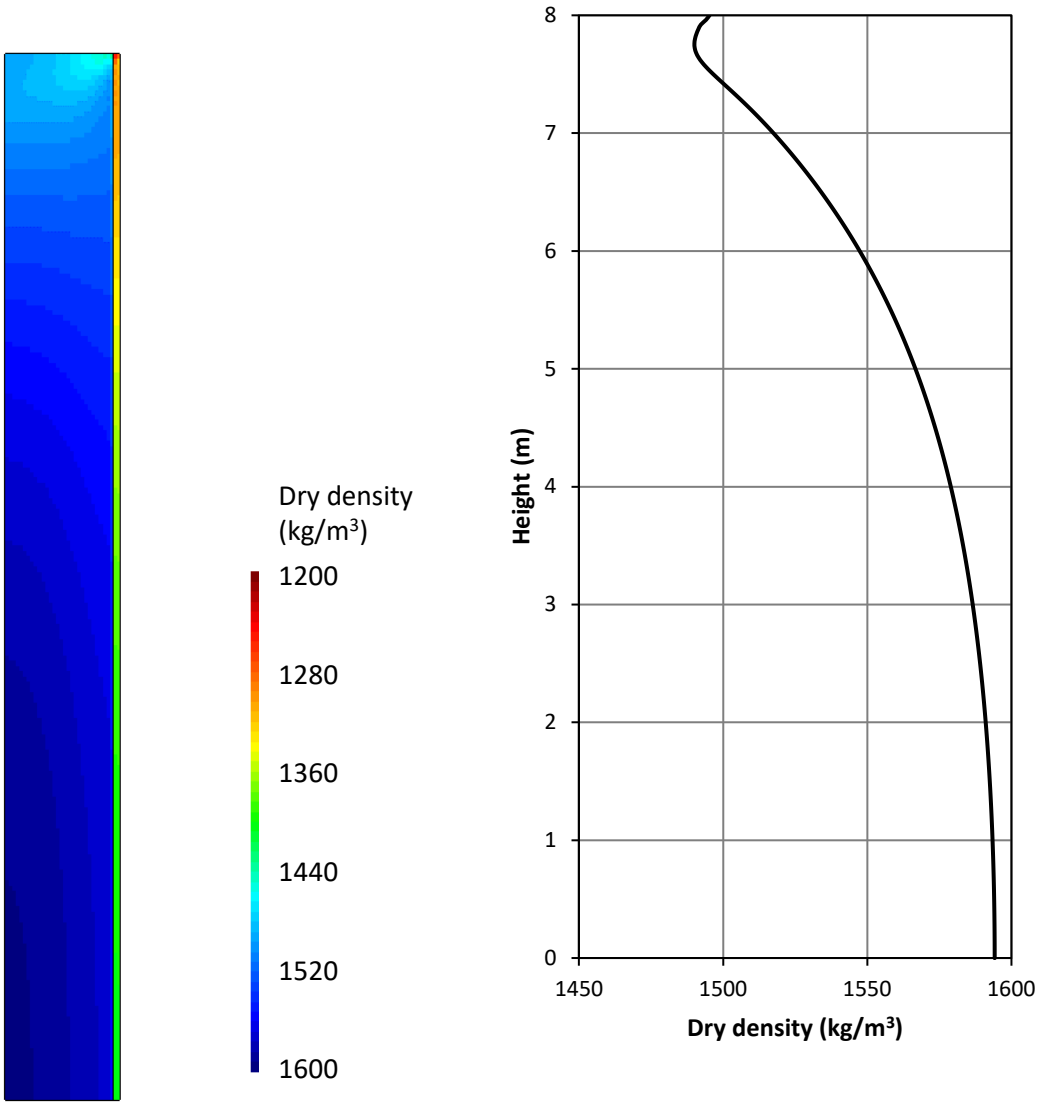

Figure 4-26. Dry density after 300 years (left). Dry density distribution at the axis after 300 years (right). Case 5.

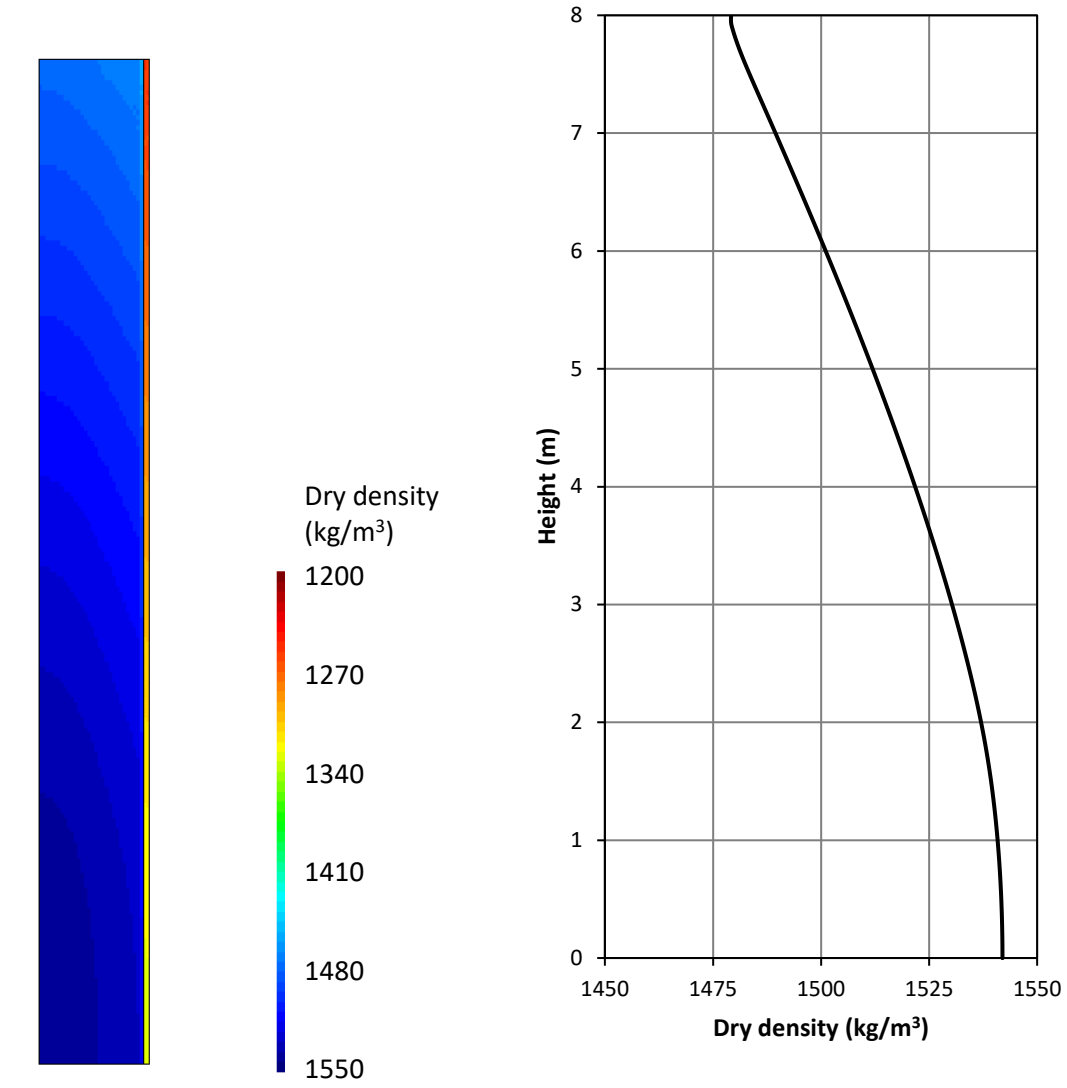

Figure 4-27. Dry density after 300 years (left). Dry density distribution at the axis after 300 years (right). Case 7.

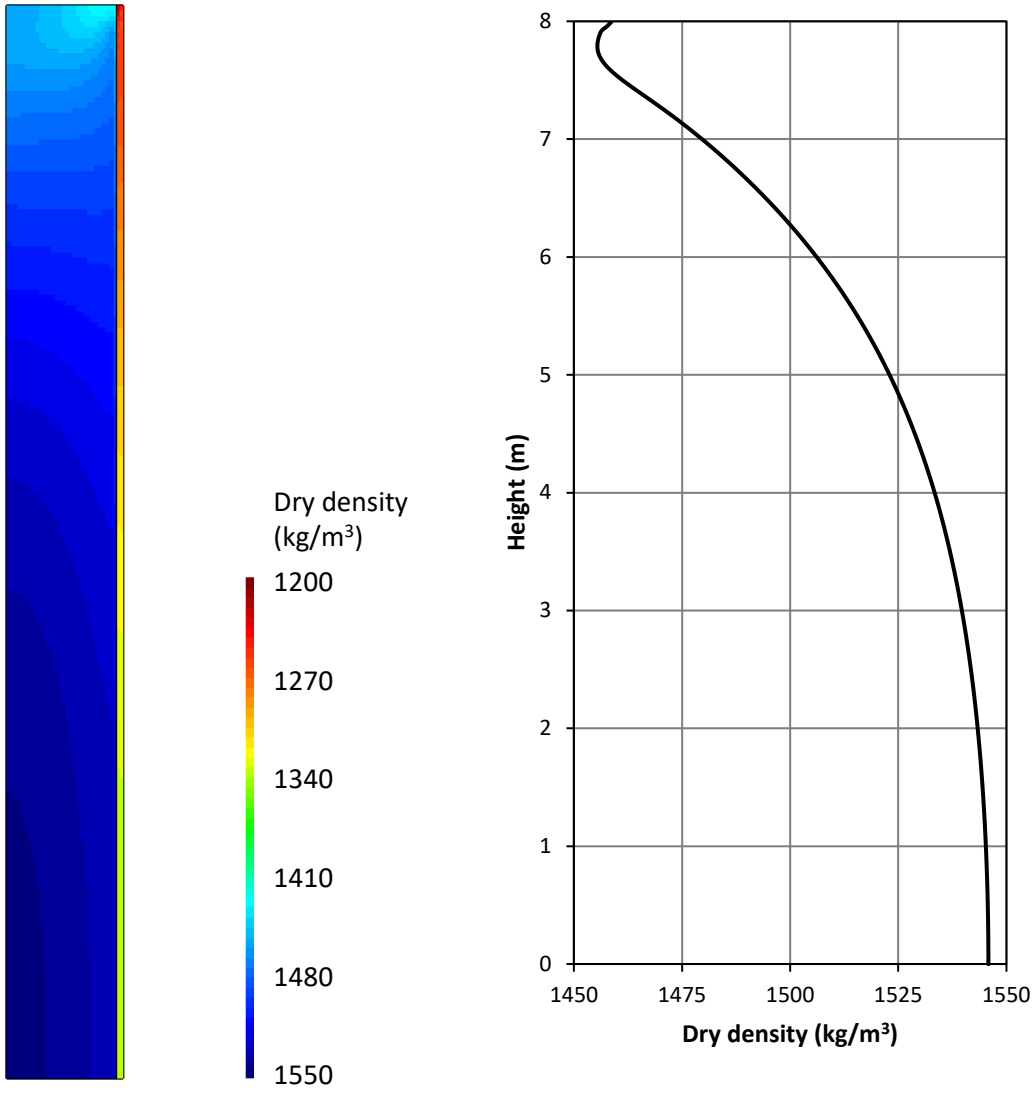

Figure 4-28. Dry density after 300 years (left). Dry density distribution at the axis after 300 years (right). Case 8.

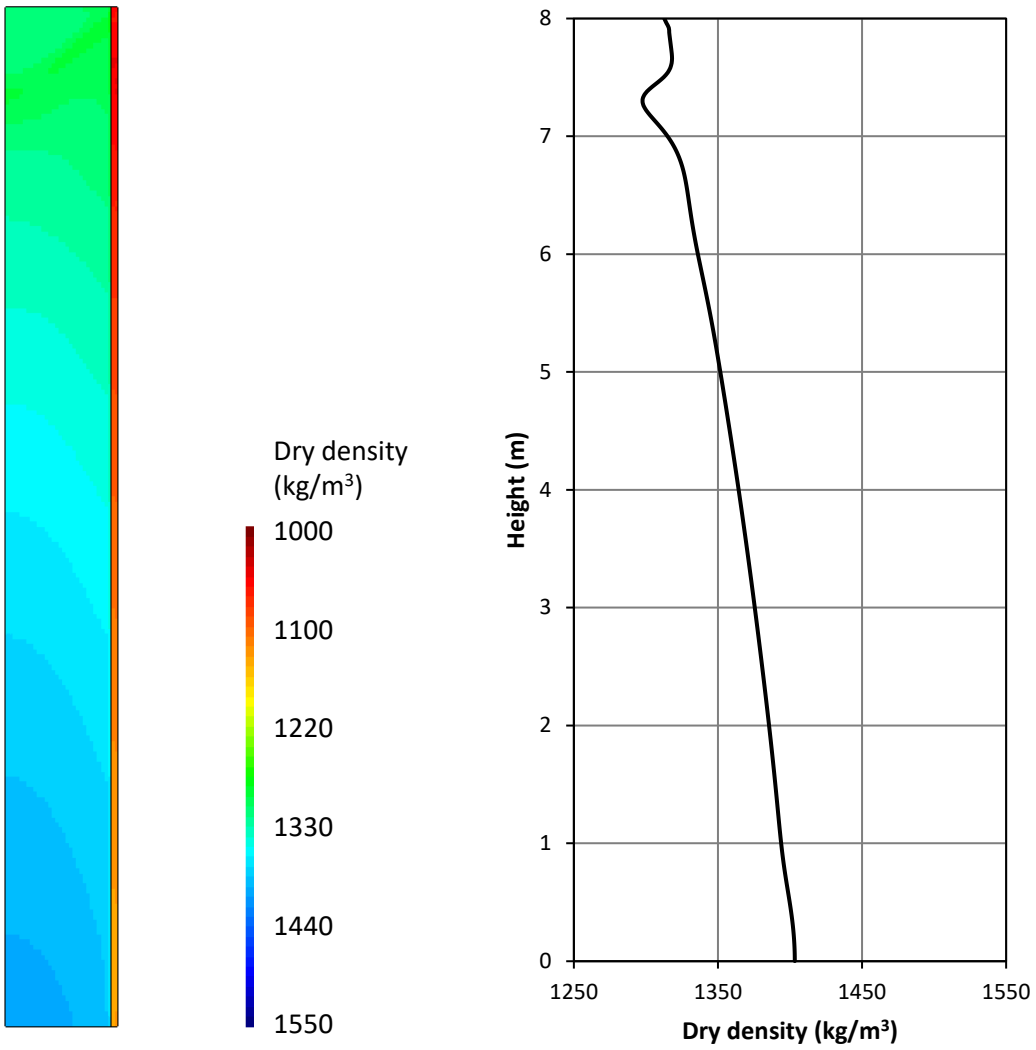

Figure 4-29. Dry density after 300 years (left). Dry density distribution at the axis after 300 years (right). Case 9.

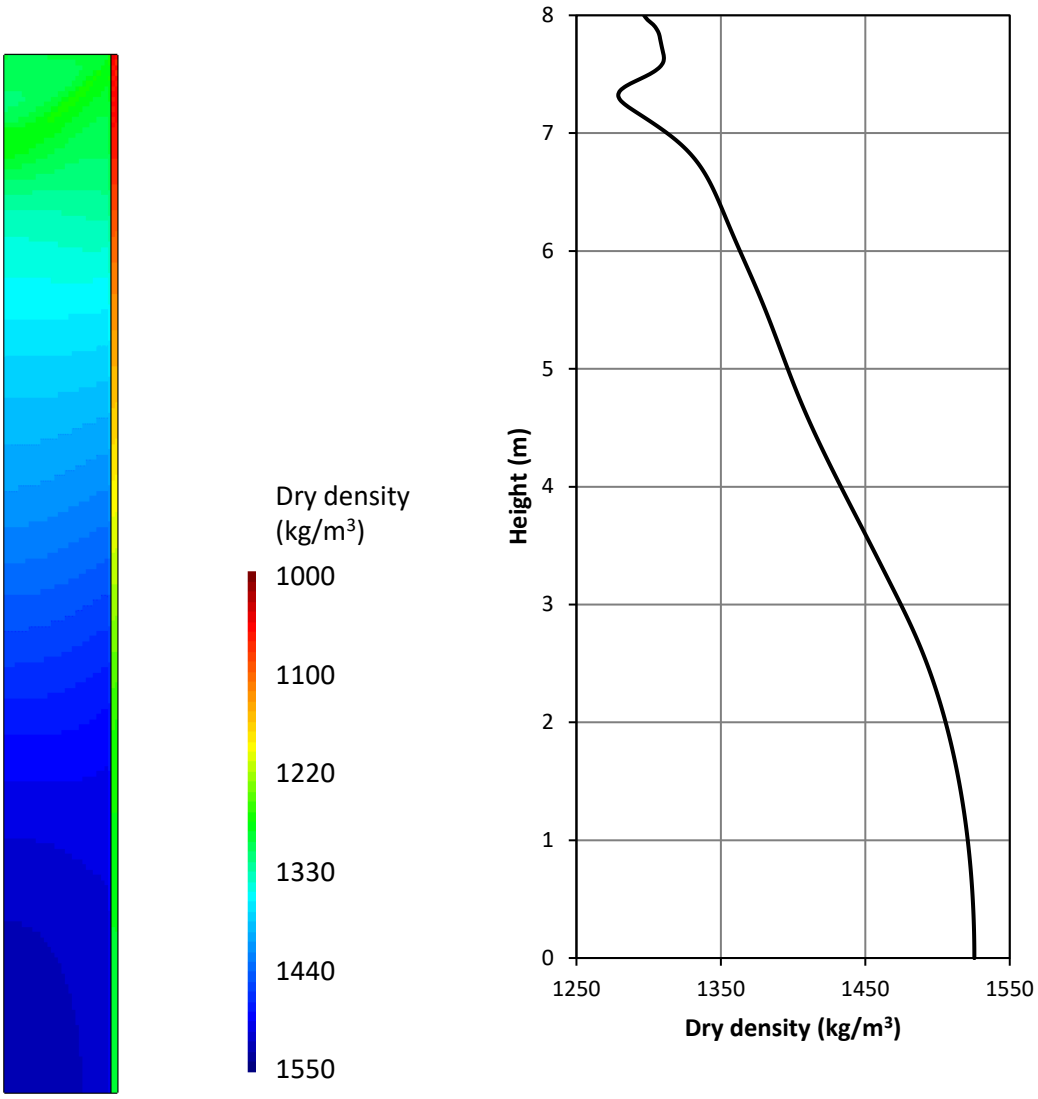

Figure 4-30. Dry density after 300 years (left). Dry density distribution at the axis after 300 years (right). Case 10.

5 Conclusions

Buffer upwards into the backfill was assessed as function of the stiffness of the backfill, water uptake boundary, density of the blocks and friction of the buffer – rock contact. The simulations were performed in axisymmetric geometry, in isothermal conditions and considering only the two components of the buffer: blocks and pellets (the canister was not simulated). One case was taken as reference (Base case) and the sensitivity analysis was performed with 9 different cases (from Case 1 to Case 10). Case 6, which assumes saturated conditions as initial condition, was not run due to the constitutive models used in this work, the Barcelona Basic Model, Alonso et al. (1990) for blocks and the Barcelona Expansive Model, Gens and Alonso (1992) for pellets, do not simulate swelling when the clays are in saturated conditions. The calculations were run in small strains setting, the updated Lagrangian was not possible to use due to convergence problems. The gravity was not considered.

The Base case was also run considering different numerical issues: tolerances, mesh size, joint thickness, joint viscosity and updated Lagrangian setting. The main differences were in buffer – rock contact, so it can be concluded that the numerical issues do not change the buffer upwards results significantly.

The Base case was also run with different constitutive models that consider the buffer – rock contact in different ways. The constitutive model chosen for the buffer – rock contact was the Drucker – Prager model implemented in CODE_BRIGHT, which is the same the Mohr – Coulomb constitutive model in some cases, and it is close when the three principal stresses are in compression.

The zero – thickness elements for the simulation of the buffer – rock contact were also checked using the Mohr – Coulomb constitutive model. Both type of elements (continuous and zero – thickness) gave similar results in plasticity and the same results in elasticity.

Finally, the continuous material and the zero-thickness elements models were run without considering the plasticity and compared with the model which considered springs in boundary (in this case, there is no material that simulates the buffer – rock contact). The results were the same but showed significant instability near the buffer – backfill boundary, where the buffer upwards displacements were the largest, especially in the zero – thickness elastic model.

The continuous elements can be used for the simulation of the friction but a deeper analysis of this model should be done. These elements behaved well and offer a wide range of constitutive models for their implementation. There is less experience with the zero – thickness elements and they are not implemented in 3-D, so the simulation of joints in 3-D geometries must be carried out with the continuous elements. For these reasons, the continuous elements are recommended for assessing the buffer – rock behaviour. The continuous elements are also the option recommended by the CODE_BRIGHT suppliers, who have prepared a document with recommendations for simulating joints with this type of elements (DECA-UPC 2020).

The results show that the backfill stiffness and blocks density are the critical parameters because their variation means large differences in buffer upwards and swelling pressure developed in the buffer – backfill contact. The buffer upwards might change from some centimetres till almost one meter and the buffer – backfill pressure from some hundreds of kPa's till some MPa's. The water supply and the friction in buffer – rock contact are not as critical as the other two parameters and the variation of the buffer upwards and swelling pressure do not change significantly when the water supply or the friction angle change.

References

SKB's (Svensk Kärnbränslehantering AB) publications can be found at www.skb.com/publications.

Alcoverro J, Pintado X, 2021. Modelling of canister shearing test using Plaxis with large strains setting. Posiva Working Report 2021-13, Posiva Oy, Finland.

Alonso E E, Gens A, Josa A, 1990. A constitutive model for partially saturated soils. Géotechnique 40, 405–430.

Brooks R H, Corey A T, 1964. Hydraulic properties of porous media. Fort Collins: Colorado State University. (Hydrology Papers 3)

Börgesson L, Johannesson L-E, Sandén T, Hernelind J, 1995. Modelling of the physical behaviour of water saturated clay barriers. Laboratory tests, material models and finite element application. SKB TR 95-20, Svensk Kärnbränslehantering AB.

Chen G J, Ledesma A, 2009. Coupled thermohydromechanical modelling of the full-scale in situ test "Prototype Repository". Journal of Geotechnical and Geoenvironmental Engineering 165, 121–132.

DECA-UPC, 2020. THM discontinuities in 2D and 3D. Department of Civil and Environmental Engineering, Universitat Politècnica de Catalunya BarcelonaTech, Spain. Available at: https://deca.upc.edu/en/projects/code_bright/downloads/documents/thm_discontinuities_3d_2d_v4.pdf

DECA-UPC, 2021. CODE_BRIGHT 2021 User's guide. A 3-D program for thermo-hydro-mechanical analysis in porous media. Department of Civil and Environmental Engineering, Universitat Politècnica de Catalunya BarcelonaTech, Spain. Available at: https://deca.upc.edu/en/projects/code_bright/downloads/users_guide/view

Dueck A, 2004. Hydro-mechanical properties of a water unsaturated sodium bentonite: laboratory study and theoretical interpretation. PhD thesis. Lund University , Sweden.

Dueck A, Nilsson U, 2010. Thermo-hydro-mechanical properties of MX-80. Results from advanced laboratory tests. SKB TR-10-55, Svensk Kärnbränslehantering AB.

Dueck A, Börgesson L, Johannesson L-E, 2010. Stress–strain relation of bentonite at undrained shear. Laboratory tests to investigate the influence of material composition and test technique. SKB TR-10-32, Svensk Kärnbränslehantering AB.

Dueck A, Goudarzi R, Börgesson L, 2016. Buffer homogenisation. Status report 3. SKB TR-16-04, Svensk Kärnbränslehantering AB.

Dueck A, Goudarzi R, Börgesson L, 2018. Buffer homogenization – status report 4. SKB TR-17-04, Svensk Kärnbränslehantering AB.

Dueck A, Börgesson L, Kristensson O, Malmberg D, Åkesson M, Hernelind J, 2019. Bentonite homogenisation. Laboratory study, model development and modelling of homogenisation processes. SKB TR-19-11, Svensk Kärnbränslehantering AB.

Gens A, Alonso E E, 1992. A framework for the behaviour of unsaturated expansive clays. Canadian Geotechnical Journal 29, 1013–1032.

Gens A, Sánchez M, Guimarães L Do N, Alonso E E, Lloret A, Olivella S, Villar M V, Huertas F, 2009. A full-scale in situ heating test for high-level nuclear waste disposal: observations, analysis and interpretation. Géotechnique 59, 377–399.

Hughes T J R, 1980. Generalisation of selective integration procedures to anisotropic and nonlinear media. International Journal for Numerical Methods in Engineering 15, 1413–1418.

Karnland O, Olsson S, Nilsson U, 2006. Mineralogy and sealing properties of various bentonites and smectite-rich clay materials. SKB TR-06-30, Svensk Kärnbränslehantering AB.

Kiviranta L, Kumpulainen S, Pintado X, Karttunen P, Schatz T, 2018. Characterization of bentonite and clay materials 2012–2015. Posiva Working Report 2016-05, Posiva Oy, Finland.

Kristensson O, Börgesson L, 2015. Canister retrieval test. Final report.
SKB TR-14-19, Svensk Kärnbränslehantering AB.

Martikainen J, Schatz T, 2011. Laboratory tests to determine the effect of Olkiluoto bounding brine water on buffer performance. Posiva Working Report 2011-68, Svensk Kärnbränslehantering AB.

Navarro V, Asensio L, De la Morena G, Pintado X, Yustres A, 2015. Differentiated intra- and inter-aggregate water content models of MX-80 bentonite. Applied Clay Science 118, 325–336.

Pintado X, Rautioaho E, 2013. Thermo-hydraulic modelling of buffer and backfill. Posiva 2012-48, Posiva Oy, Finland.

Pintado X, Hassan M M, Martikainen J, 2013. Thermo-hydro-mechanical tests of buffer material. Posiva 2012-49, Posiva Oy, Finland.

Pintado X, Kristensson O, Malmberg D, Åkesson M, Olivella S, Puig I, 2018. TH and THM modelling of a KBS-3H deposition drift. Posiva working Report 2016-25, Posiva Oy, Finland.

Rodríguez-Dono A, Olivella S, Mokni N, 2020. Assessment of a high-level spent nuclear fuel disposal model. Environmental Geotechnics 7, 42–58.

Sandén T, Kristensson O, Lönnqvist M, Börgesson L, Nilsson U, Goudarzi R, 2020. Buffer swelling. Laboratory tests and modelling. SKB TR-20-04, Svensk Kärnbränslehantering AB.

Schatz T, Martikainen J, 2011. Laboratory studies on the effect of freezing and thawing exposure on bentonite buffer performance: Closed-system tests. Posiva 2010-06, Posiva Oy, Finland.

Seiphoori A, 2014. Thermo-hydro-mechanical characterisation and modelling of MX-80 granular bentonite. PhD thesis. École Polytechnique Fédérale de Lausanne, Switzerland.

Sinnathamby G, Korkiala-Tanttu L, Gallardo Forés J, 2014. Interface shear behaviour of tunnel backfill materials in a deep-rock nuclear waste repository in Finland. Soils and Foundations 54, 777–788.

Tang A-M, 2005. Effet de la température sur le comportement des barrières de confinement. PhD thesis. École Nationale des Ponts et Chausées, Paris, France.

Toprak E, 2018. Long term response of multi-barrier schemes for underground radioactive waste disposal. PhD thesis. Technical University of Catalonia. Barcelona, Spain.

Toprak E, Mokni N, Olivella S, Pintado X, 2013. Thermo-hydro-mechanical modelling of buffer. Synthesis report. Posiva 2012-47, Posiva Oy, Finland.

Toprak E, Olivella S, Pintado X, 2016. Coupled THM modelling of engineered barriers for the final disposal of spent nuclear fuel isolation. Geological Society, London, Special Publications 443, 235–251.

Toprak E, Olivella S, Pintado X, 2018. Modelling engineered barriers for spent nuclear fuel repository using a double structure approach for pellet-based components. Journal of Environmental Geotechnics 7, 72–94.

van Genuchten M T, 1980. A closed-form equation for predicting the hydraulic conductivity of unsaturated soils. Soil Science Society American Journal 44, 892–898.

van Langen R, 1991. Numerical analysis of soil-structure interaction. PhD thesis. Delft University of Technology, The Netherlands.

Villar M V, 2005. MX-80 bentonite. Thermo-hydro-mechanical characterization performet at CIEMAT in the context of the prototype project. Technical Report CIEMAT/DIAE/54540/2/04, CIEMAT, Madrid, Spain.

Villar M V, 2007. Water retention of two natural compacted bentonites. Clays and Clay Minerals 55, 311–322.

Zandarin M T, 2010. Thermo-hydro-mechanical analysis of joints. A theoretical and experimental study. PhD thesis. Technical University of Catalonia, Barcelona, Spain.

Zandarin M T, Gens A, Olivella S, Alonso E E, 2011. Thermo-hydro-mechanical model of the Canister Retrieval Test. Physics and Chemistry of the Earth 36, 1806–1816.

Åkesson M, Jacinto A-C, Gatabin C, Sánchez M, Ledesma A, 2009. Bentonite THM behaviour at high temperatures: experimental and numerical analysis. Géotechnique 59, 307–318.

Åkesson M, Kristensson O, Börgesson L, Dueck A, Hernelind J, 2010. THM modelling of buffer, backfill and other system components. Critical processes and scenarios. SKB TR-10-11, Svensk Kärnbränslehantering AB.

Appendix 1

Oedometer test analysis in large strains settings

The oedometer test results obtained with three different rates have been compared (see Figure A-1; van Langen 1991). Note that the logarithmic strain is used.

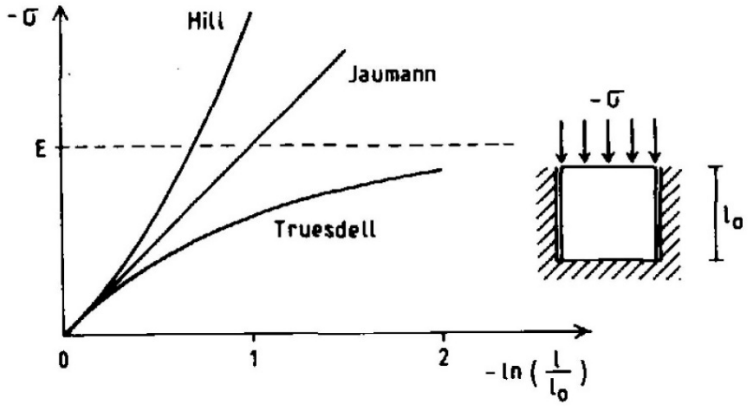

Figure A-1. *Result of oedometer test for three stress rate definitions (van Langen, 1991).*

The generic constitutive equation of an isotropic linear-elastic material is

$$\mathring{\boldsymbol{\sigma}} = \lambda(tr\mathbf{D})\mathbf{I} + 2\mu\mathbf{D} \tag{A-1}$$

where is $\mathring{\boldsymbol{\sigma}}$ an objective rate of the Cauchy stress (Jaumann, Truesdell or Hill) and the parameters λ and μ are the Lamé moduli, given by the equations

$$\begin{aligned} \lambda &= \frac{E\nu}{(1+\nu)(1-2\nu)} \\ \mu &= \frac{E}{2(1+\nu)} \end{aligned} \tag{A-2}$$

where E is the Young modulus and ν is the Poisson ratio. If ν=0, the considered generic constitutive equation reduces to

$$\mathring{\boldsymbol{\sigma}} = E\mathbf{D} \tag{A-3}$$

The kinematics of the oedometer test can be defined as:

$$\begin{aligned} x_1 &= (1-t)X_1 \\ x_2 &= X_2 \\ x_3 &= X_3 \end{aligned} \tag{A-4}$$

where $0 \leq t < 1$. Consequently, the deformation gradient $\mathbf{F}$ reads

$$\mathbf{F} = (1-t)\,\mathbf{e_1} \otimes \mathbf{e_1} + \mathbf{e_2} \otimes \mathbf{e_2} + \mathbf{e_3} \otimes \mathbf{e_3} = \begin{bmatrix} 1-t & 0 & 0 \\ 0 & 1 & 0 \\ 0 & 0 & 1 \end{bmatrix} \tag{A-5}$$

And the spatial velocity gradient $\mathbf{L}(t) = \dot{\mathbf{F}}(t)\mathbf{F^{-1}}(t)$

$$\mathbf{L} = \frac{-1}{1-t}\,\mathbf{e_1} \otimes \mathbf{e_1} = \begin{bmatrix} \frac{-1}{1-t} & 0 & 0 \\ 0 & 0 & 0 \\ 0 & 0 & 0 \end{bmatrix} = \dot{\varepsilon}(t)\,\mathbf{e_1} \otimes \mathbf{e_1} \begin{bmatrix} \dot{\varepsilon}(t) & 0 & 0 \\ 0 & 0 & 0 \\ 0 & 0 & 0 \end{bmatrix} \quad \text{A-6}$$

Where ε is the axial logarithmic strain, defined by

$$\varepsilon(t) = log(1-t) \quad \text{A-7}$$

Hence, the stretching tensor $\mathbf{D}$ and the spin tensor $\mathbf{W}$ read

$$\mathbf{D} = \dot{\varepsilon}(t)\,\mathbf{e_1} \otimes \mathbf{e_1} = \begin{bmatrix} \dot{\varepsilon}(t) & 0 & 0 \\ 0 & 0 & 0 \\ 0 & 0 & 0 \end{bmatrix}; \mathbf{W}=\mathbf{0} \quad \text{A-8}$$

Solution with the Jaumann rate

The Jaumann rate of the Cauchy stress tensor reads

$$\overset{\circ J}{\boldsymbol{\sigma}} = \dot{\boldsymbol{\sigma}} - \mathbf{W} \cdot \boldsymbol{\sigma} + \boldsymbol{\sigma} \cdot \mathbf{W} \quad \text{A-9}$$

Using $\boldsymbol{W}(t) = \mathbf{0}$, this relation reduces to

$$\overset{\circ J}{\boldsymbol{\sigma}} = \dot{\boldsymbol{\sigma}} \quad \text{A-10}$$

which substituted in the constitutive equation yields

$$\dot{\boldsymbol{\sigma}} = E\mathbf{D} \quad \text{A-11}$$

Since the only non-vanishing component of $\mathbf{D}(t)$ is $D_{11}(t) = \dot{\varepsilon}(t)$, the constitutive equation shows that $\sigma_{11}(t)$ satisfies the relation $\dot{\sigma}_{11}(t) = E\ \dot{\varepsilon}(t)$.

For a monotonic process (extension $\dot{\varepsilon}(t) > 0$ or compression $\dot{\varepsilon}(t) < 0$), time *t* can be replaced by the axial logarithmic strain ε, resulting in $\sigma_{11}^{'} = E$

where the notation $()^{'} = \frac{d}{d\varepsilon}()$ is used. The solution of this ordinary differential equation reads:

$$\sigma_{11}(\varepsilon) = \sigma_{11}(0) + E\varepsilon \quad \text{A-12}$$

If at the initial state ($\varepsilon(0) = log(1-0) = 0$) and $\sigma_{11}(0) = 0$, this expression reduces to

$$\sigma_{11}(\varepsilon) = E\varepsilon \quad \text{A-13}$$

Solution with the Truesdall rate

The Truesdell rate of the Cauchy stress tensor reads

$$\overset{\circ T}{\boldsymbol{\sigma}} = \dot{\boldsymbol{\sigma}} - \mathbf{L} \cdot \boldsymbol{\sigma} - \boldsymbol{\sigma} \cdot \mathbf{L}^T + tr(\mathbf{D})\boldsymbol{\sigma} \quad \text{A-14}$$

Using $\mathbf{W}(t) = \mathbf{0}$, this relation reduces to

$$\overset{\circ T}{\boldsymbol{\sigma}} = \dot{\boldsymbol{\sigma}} - \mathbf{D} \cdot \boldsymbol{\sigma} - \boldsymbol{\sigma} \cdot \mathbf{D} + tr(\mathbf{D})\boldsymbol{\sigma} \quad \text{A-15}$$

which substituted in the constitutive equation yields

$$\dot{\boldsymbol{\sigma}} - \mathbf{D}\cdot\boldsymbol{\sigma} - \boldsymbol{\sigma}\cdot\mathbf{D} + tr(\mathbf{D})\boldsymbol{\sigma} = E\mathbf{D} \qquad \text{A-16}$$

Since the only non-vanishing component of $\boldsymbol{D}(t)$ is $D_{11}(t) = \dot{\varepsilon}(t)$, the constitutive equation shows that $\sigma_{11}(t)$ satisfies the relation

$$\dot{\sigma}_{11}(t) - \dot{\varepsilon}(t)\sigma_{11}(t) = E\ \dot{\varepsilon}(t) \qquad \text{A-17}$$

For a monotonic process (extension $\dot{\varepsilon}(t) > 0$ or compression $\dot{\varepsilon}(t) < 0$), time *t* can be replaced by the axial logarithmic strain ε, resulting in $\sigma_{11}^{'} - \sigma_{11} = E$

where the notation $()^{'} = \frac{d}{d\varepsilon}()$ is used. The solution of this ordinary differential equation reads:

$$\sigma_{11}(\varepsilon) = \sigma_{11}(0)e^{\varepsilon} + E(e^{\varepsilon} - 1) \qquad \text{A-18}$$

If at the initial state ($\varepsilon(0) = log(1 - 0) = 0$) $\sigma_{11}(0) = 0$, this expression reduces to

$$\sigma_{11}(\varepsilon) = E(e^{\varepsilon} - 1) \qquad \text{A-19}$$

Solution with the Hill rate

The Hill rate of the Cauchy stress tensor reads

$$\overset{\circ H}{\boldsymbol{\sigma}} = \dot{\boldsymbol{\sigma}} - \mathbf{W}\cdot\boldsymbol{\sigma} + \boldsymbol{\sigma}\cdot\mathbf{W} + tr(\mathbf{D})\boldsymbol{\sigma} \qquad \text{A-20}$$

Using $\mathbf{W}(t) = \mathbf{0}$, this relation reduces to

$$\overset{\circ H}{\boldsymbol{\sigma}} = \dot{\boldsymbol{\sigma}} + tr(\mathbf{D})\boldsymbol{\sigma} \qquad \text{A-21}$$

which substituted in the constitutive equation yields

$$\dot{\boldsymbol{\sigma}} + tr(\mathbf{D})\boldsymbol{\sigma} = E\mathbf{D} \qquad \text{A-22}$$

Since the only non-vanishing component of $\mathbf{D}(t)$ is $D_{11}(t) = \dot{\varepsilon}(t)$, the constitutive equation shows that $\sigma_{11}(t)$ satisfies the relation

$$\dot{\sigma}_{11}(t) + \dot{\varepsilon}(t)\sigma_{11}(t) = E\ \dot{\varepsilon}(t) \qquad \text{A-23}$$

For a monotonic process (extension $\dot{\varepsilon}(t) > 0$ or compression $\dot{\varepsilon}(t) < 0$), time t can be replaced by the axial logarithmic strain ε, resulting in $\sigma_{11}^{'} + \sigma_{11} = E$

where the notation $()^{'} = \frac{d}{d\varepsilon}()$is used. The solution of this ordinary differential equation reads:

$$\sigma_{11}(\varepsilon) = \sigma_{11}(0)e^{-\varepsilon} + E(1 - e^{-\varepsilon}) \qquad \text{A-24}$$

If at the initial state ($\varepsilon(0) = log(1 - 0) = 0$) and $\sigma_{11}(0) = 0$, this expression reduces to

$$\sigma_{11}(\varepsilon) = E(1 - e^{-\varepsilon}) \qquad \text{A-25}$$

Solution with the material derivative rate. Large strains setting used in CODE_BRIGHT

The (non-objective) material derivative rate of the Cauchy stress tensor is $\dot{\boldsymbol{\sigma}}$ which substituted in the constitutive equation yields

$$\dot{\boldsymbol{\sigma}} = E\mathbf{D} \qquad \text{A-26}$$

Since the only non-vanishing component of $\boldsymbol{D}(t)$ is $D_{11}(t) = \dot{\varepsilon}(t)$, the constitutive equation shows that $\sigma_{11}(t)$ satisfies the relation

$$\dot{\sigma}_{11} = E\dot{\varepsilon}(t) \qquad \text{A-27}$$

For a monotonic process (extension $\dot{\varepsilon}(t) > 0$ or compression $\dot{\varepsilon}(t) < 0$), time *t* can be replaced by the axial logarithmic strain ε, resulting in

$$\sigma_{11}^{'} = E \qquad \text{A-28}$$

where the notation $()^{'} = \frac{d}{d\varepsilon}()$ is used. The solution of this ordinary differential equation reads:

$$\sigma_{11}(\varepsilon) = \sigma_{11}(0) + E\varepsilon \qquad \text{A-29}$$

If at the initial state ($\varepsilon(0) = log(1 - 0) = 0$) and $\sigma_{11}(0) = 0$, this expression reduces to

$$\sigma_{11}(\varepsilon) = E\varepsilon \qquad \text{A-30}$$

Which is the expression obtained with the Jaumann rate.

PLAXIS uses the Hill rate because it reproduces better this test (see Figure A-1).

This test has been simulated with CODE_BRIGHT (1×1 m in plane strain) and compared with the results obtained from the analytical results obtained with the rates of Hill, Truesdell and Jaumann, which is equivalent to the large strains setting used in CODE_BRIGHT (for this test). The results can be seen in Figure A-2.

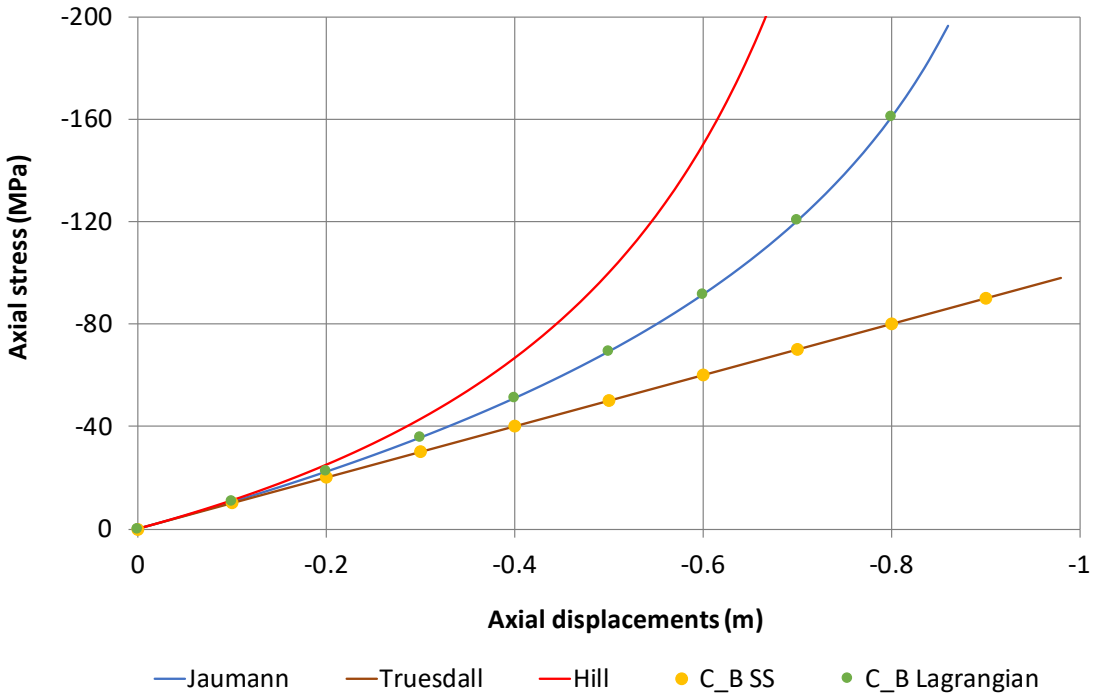

Figure A-2. *Result of oedometer test for three stress rate definitions.*

The small strains setting in CODE_BRIGHT is equivalent to Truesdall rate and the large strains setting is equivalent to Jaumann rate.

More analyses of the large strains setting in laboratory tests can be found in Pintado, X. 2019. CODE_BRIGHT small strains verification. Internal Posiva memorandum POS-032444. Eurajoki, Finland.